Master's thesis

NTNU
Norwegian University of Science and Technology
Faculty of Engineering
Department of Energy and Process Engineering

Frida Sæther

Development of an Intermediate PCM Storage for a Wood Stove

A numerical study

Master's thesis in Energy and Environmental Engineering
Supervisor: Erling Næss
Co-supervisor: Alexis Sevault, Geir Hansen
June 2022

NTNU
Norwegian University of
Science and Technology

Frida Sæther

Development of an Intermediate PCM Storage for a Wood Stove

A numerical study

Master's thesis in Energy and Environmental Engineering
Supervisor: Erling Næss
Co-supervisor: Alexis Sevault, Geir Hansen
June 2022

Norwegian University of Science and Technology
Faculty of Engineering
Department of Energy and Process Engineering

NTNU
Norwegian University of
Science and Technology

Preface

This thesis is my Master's thesis which is written for the Department of Energy and Process Engeneering at the Norwegian University of Science and Technology (NTNU). The thesis investigates possible enhancements for both inner and outer heat transfer for an already constructed storage design. The study is based on simplified estimations followed by more comprehensive numerical computations.

The work conducted is a contribution to an ongoing research and innovation project named IPN PCM-STOVE. The aim is to develop a latent heat thermal energy storage to be used for intermediate heat storage in modern wood stoves. It is a project supported by the Research Council of Norway and an industrial partner.

I would like to express my sincere gratitude and appreciation to my supervisors; Professor Erling Næss at NTNU, Research Scientist Alexis Sevault at SINTEF Energy, and Geir Hansen at NTNU, for the guidance and interesting discussions concerning my work during this master's thesis. The learning outcome has been huge, and I am ending this epoch with great motivation to embark the next chapter in life.

Frida Sæther

Frida Sæther, Trondheim, June 9 2022

Abstract

Norwegian households' heating demand is mainly supplied by electricity. A more sustainable way of providing heat to households for room heating is to utilize modern wood stoves. Due to the modern passive houses' low heating demand, a nominal duty of 5kW supplied from a typical wood stove would supply a too large duty. An attractive technology to solve this problem is to utilize an intermediate heat storage using a phase change material.

Before this master's thesis, several investigations and reports have been carried out as pieces of an innovative research project. This project aims to develop a latent heat thermal energy storage suitable for a modern wood stove used in a typical Norwegian home.

A pilot has previously been developed and tested in the laboratory. Its performance was inadequate in not releasing the desired amount of heat approximated to 6 kWh during the desired discharge duration of 8 hours. A large thermal resistance was observed outside the storage container, resulting in an inefficient heat release. A design modification was carried out as a result of this thesis, where 16 channels were attached to the vertical container wall. These channels helped with a larger heat transfer area, decreasing the outer thermal resistance. The heat released during 8 hours increased from 5.4 kWh to 6.1 kWh, which was a 13 % increase resulting in the desired heat being released during the desired duration.

Another challenge regarding the existing thermal energy storage is the low degradation temperature of 300 °C for the phase change material. Since the magnitude of the heat fluxes that might occur at the storage bottom during a firing process is unknown, the risk of overheating the material is assumed to be large due to the material's low thermal conductivity. An experimental, numerical study using computational software has been conducted to see how significant an increase in heat fluxes a phase change material would endure by obtaining natural convection. A Rayleigh number exceeding 1708 is required for an infinite cavity to onset natural convection. An estimation of which material properties would onset natural convection was conducted as a base before a more comprehensive, numerical study was carried out. The approach was to compute different scenarios of melted volumes with fixed heights to see how altering the material's properties would affect the occurrence of natural convection and an increase in tolerable heat fluxes. By experimenting with different density changes caused by a temperature difference, and different dynamic viscosities, a concoct material was able to possibly tolerate a 4.34 times larger heat flux without risking the bottom temperature to reach its critical temperature. This heat flux was compared to if the heat was only transferred through conduction.

Several suggestions on further work of interest have been mentioned. Among them, a suggestion is to perform another numerical simulation of the discharge process for the storage where a more realistic surrounding temperature would be present to observe how this will increase the discharge duration. Also, a study where the actual heat fluxes obtained at the storage bottom are measured would be of great interest. Such investigation may imply whether the perceived risk of overheating the phase change material is genuine.

Sammendrag

Norske husholdningers varmebehov blir hovedsakelig dekt av elektrisitet. En mer bærekraftig energikilde til romoppvarming ville vært og benyttet en moderne vedovn. På grunn av de moderne passivhusenes lave varmebehov vil den nominelle effekten på 5kW levert av en typisk vedovn levere alt for høy effekt. En attraktiv teknologi som en løsning på dette problemet kan være å introdusere et midlertidig varmelager som benytter et faseendringsmateriale.

I forkant av denne masterstudien var det allerede gjort flere studier som alle var bidrag til et forskning- og innovasjonsprosjekt. Formålet med prosjektet er å utvikle et termisk energilager som utnytter latent varme hos et materiale som skal festes til en vedovn.

En prototype er allerede blitt utviklet og testet i laboratoriet. Prototypen indikerte at ønsket mengde energi på omtrent 6kWh ikke ble levert i løpet av en ønsket utladningsperiode på 8 timer. En stor termisk motstand ble sagt å befinne seg på lagerets utside som resulterte i en ineffektiv varmeavgivelse. Et modifisert lagerdesign har blitt fremstilt som et resultat av denne masteroppgaven hvor 16 vertikale kanaler ble festet på lagerets ytre vegg. Disse kanalene bidro til å minke den termiske motstanden ved å øke lagerets ytre overflateareal. Varmen avgitt i løpet av 8 timer økte fra 5.4 kWh til 6.1 kWh. Dette var en økning på 13 % og resulterte i at ønsket mengde energi ble avgitt i løpet av antall ønsket timer.

En annen utfordring ved den eksisterende prototypen er faseendringsmaterialets relativt lave degraderingstemperatur. Ettersom det er uvisst hvor høye varmeflukser som muligens kan oppstå på bunnen av lageret, er risikoen for å oppnå degradering av materialet antatt å være høy på grunn av materialets lave konduktivitet. En eksperimentell studie er gjort ved bruk av en programvare som løser fluiddynamikk-problemer numerisk. Studien gikk ut på å se hvor store økninger i varmefluks et materiale ville tåle om frikonveksjon var til stede i materialet ved samme grensebetingelser. For et uendelig stort domene, må materialets strømning overgå et Rayleigh nummer på 1708 for at frikonveksjon skal oppstå. Først ble det undersøkt hvor store varmeflukser ulike smeltevolum med gitte høyder ville tåle om varmen kun ble ledet gjennom ved hjelp av konduksjon. Disse resultatene ble brukt som sammenligningsgrunnlag når ulike scenarioer med frikonveksjon ble simulert og høyere varmeflukser ble observert. Studien ble gjort ved å eksperimentere med ulike tetthetsendringer som var et resultat av temperaturforskjellen mellom bunn og topp av smeltevolumet, i tillegg til at to ulike dynamiske viskositeter ble antatt. Ett av resultatene viste at ved å ha et materiale som opplever frikonveksjon på grunn av tetthetsendringer, en varmefluks påsatt ved bunnen av lageret kunne bli økt med en faktor på 4.34 uten at materialet ville nærmet seg degraderingstemperaturen.

Flere forslag til videre arbeid er blitt nevn til slutt. Blant disse, er et av forslagene å simulere en ny utladningsprosess for det modifiserte lagerdesignet med en mer realistisk omgivelsestemperatur. En høyere temperatur er antatt i begynnelsen, noe som vil føre til lengre utladningstid. I tillegg er det av interesse å måle et faktisk tidsforløp av varmefluksen som vil oppstå mellom toppen av ovnen og lagerbunnen. Resultatene fra en slik undersøkelse kan indikere om risikoen for å overhete faseendringsmaterialet er så stor som fryktet eller ikke.

Contents

Abstract **iii**

Sammendrag **v**

List of Figures **xi**

List of Tables **xiii**

1 Introduction **1**

1.1 Objectives 2

1.2 Structure 2

2 Overview of PCM Applications **5**

2.1 Industrial Applications 5

2.1.1 Application of PCM in Mobilized-Thermal Energy Storage 5

2.2 Building Applications 6

2.2.1 Office Wall Containing PCM for Cooling 7

2.3 Food Applications 7

2.3.1 Food Storing 7

2.3.2 Food Processing 7

2.4 Electronic Chip Applications 8

2.4.1 Thermal Management of a Mobile Device 8

3 Concept and Design **11**

4 Outer Heat Transfer **15**

4.1 Estimating an Optimum Channel Arrangement . . . 16
4.1.1 Radiation . . . 16
4.1.2 Natural Convection on External Surfaces . . . 17
4.1.3 Convective Heat Transfer Inside a Channel . . . 18
4.1.4 Resulting Channel Arrangement . . . 22
4.2 Investigating Effects from Tubes Through the Storage . . . 25
4.3 Numerical Computation on Channel Flow . . . 25
4.3.1 Geometry and Meshing . . . 25
4.3.2 Models . . . 27
4.3.3 Boundary Conditions . . . 27
4.3.4 Numerical Results . . . 28
4.4 Change in Discharge Period . . . 30
4.4.1 Method . . . 31
4.4.2 Results . . . 32
4.5 Discussion . . . 34
4.5.1 Analyzing the Plots from the Channel Optimizations . . . 34
4.5.2 Obtained "Optimal" Channel . . . 36
4.5.3 Deviation Between Estimated and Numerical Results . . . 36
4.5.4 Discharge Period . . . 37
4.6 Conclusion . . . 38

5 Inner Heat Transfer 39
5.1 Onset Natural Convection . . . 39
5.2 Estimating PCM Properties to Onset Natural Convection . . . 40
5.2.1 Method . . . 41
5.2.2 Results . . . 42
5.3 Numerical Computation of Enhanced Inner Heat Transfer . . . 43
5.3.1 Geometry and Meshing . . . 43
5.3.2 Models . . . 44
5.3.3 Boundary conditions . . . 44

5.3.4 Results 45

5.4 Discussion 48

5.4.1 Conditions Representing Onset of Natural Convection 48

5.4.2 Effects from Increasing Density Gradient 49

5.4.3 Increase in Tolerable Heat Flux 49

5.4.4 Relevant CAD-model 49

5.4.5 Reliability of the Numerical Results 50

5.4.6 Choice of Viscosity 51

5.4.7 Realistic Charging Behavior 51

5.5 Conclusion 51

6 Conclusion **53**

6.1 Enhanced Outer Heat Transfer 53

6.2 Enhanced Inner Heat Transfer 54

7 Further work **57**

Bibliography **59**

Appendix **A-1**

A Additional Results from Channel Estimations A-1

A.1 Heat Transfer Obtained from the Outer Extended Surface A-1

A.2 Heat Transfer Obtained Through the Channel A-2

B Heat Transfer Coefficient (HTC) B-1

C Thermal properties for HDPE C-1

C.1 Specific heat capacity C-1

C.2 Thermal conductivity C-2

C.3 Constant properties C-2

D Container Properties D-1

E Matlab Code from Channel Estimations E-1

F Effective Conductivity for Air Void in Storage F-1

G Proportional Relations for Natural Convection G-1
G.1 Derivation G-1
G.2 Plot of the Obtained Constants G-2

List of Figures

2.1 This is the sketch of the storage tanks used in the article *"Economic efficiency of mobile latent heat storages"*[11]. 6

2.2 This is the schematic diagram shown in the article *"Use of latent heat storage to conserve energy during drying and its effect on drying kinetics of a food product"* of the drying system using a latent heat system[15]. . . 8

2.3 Sketches of the concept in *"Experimental and numerical study on phase change material (PCM) for thermal management of mobile devices"*[19]. . . 9

3.1 Sketch of the TES placement and the inside of the exiting laboratory pilot. 11

3.2 Sketch of how the channel arrangement may look like. 12

4.1 Principle sketch of the vertical cross section of one channel obtained between the inner storage surface and the external wall. 15

4.2 Sketch of the top view of channels obtained between the inner and external storage walls. 20

4.3 Sketch of the fin approach for calculating the temperature distribution in the external wall. 20

4.4 Estimated total heat transfer from the LHTES when the inner surface holds a uniform temperature of 60 °C. The different graphs represents different number of fins (N). 23

4.5 CAD-model representing one out of 16 channels constituting the vertical storage wall. 26

4.6 Graphs from the mesh independence study conducted on the channel flow. 26

4.7 Close up on the volume mesh generated for the channel calculations. 27

4.8 The two CAD models used to compute the discharge process for the LHTES without and with channels. 31

4.9 Numerical results of the total heat from the storage during discharge. The graphs pictures the discharge process for a storage with and without channels. 33

4.10 Numerical results of the change in average PCM temperature in the storage during discharge. The graphs pictures the discharge process for a storage with and without channels. 33

5.1 Sketch of the melted PCM volume during charging. The volume height increases as the PCM melts due to heat supplied at the bottom. 40

5.2 Graphs from the mesh independence study conducted on the 5cm tall melting volume. 44

5.3 These graphs present the effective conductivity obtained in a melted PCM of 5 cm height for a variety of density gradients between bottom and top for two different viscosities. 45

5.4 Pathlines obtained from the fluid motion of the melted HDPE. 46

5.5 A graphical representation of the simulated results. The relative thermal conductivity obtained for different melting height when the density gradient between top and bottom is 60 kg/m^3. 47

5.6 Pictures of the different fluid pattern for two different melting heights. . . . 48

A.1 Heat release from outer surface as a function of slit distance. The different curves represent different number of fins attaching the extended surface to the storage. A-1

A.2 Heat exchange through the channel as a function of slit distance. The different curves represent different number of fins attaching the extended surface to the storage. A-2

B.1 HTC at a vertical wall as a function of surface temperature. B-1

B.2 HTC at a horizontal wall as a function of surface temperature. B-1

C.1 Graph picturing the piece-wise linear function for specific heat capacity. . . C-1

C.2 Graph picturing the piece wise linear function of thermal conductivity for the HDPE. C-2

F.1 Expression for effective thermal conductivity for the air void represented as a solid in the numerical computations. This was derived from experimental data. F-1

G.1 Every single proportionality constant for the relative thermal conductivity and characteristic length. A constant is computed for each simulated scenario. They are calculated from the numerical results obtained in chapter 5. G-2

List of Tables

4.1 Friction factor and Nusselt number for different aspect ratios for a rectangula duct. The aspect ratio is the ratio between the average of inner and outer channel wall, *b*, and the slit distance, *a*. These tabulated numbers apply for uniform surface temperatures and for a laminar and fully developed flow. 19

4.2 Summary of estimations for a cast iron container at 60 °C. The peak of heat transfer curve for each number of fins are reproduced. 23

4.3 Summary of estimations for an aluminum container at 60 °C. The peak of heat transfer curve for each number of fins are reproduced. 23

4.4 This summarizes the most important results for the estimated heat transfer when the inner storage surface holds 200 °C. 24

4.5 Estimated and numerical results of the channel performance when the inner surface hold a temperature of 60 °C. 28

4.6 Estimated and numerical results of the channel performance when the inner surface hold a temperature of 200 °C. 29

4.7 Numerical results when including radiation in the channel computations when the inner surface hold a temperature of 60 °C. The change in results by including radiation compared to neglecting it is also presented. 30

4.8 Numerical results when including radiation in the channel computations when the inner surface hold a temperature of 200 °C. The change in results by including radiation compared to neglecting it is also presented. 30

5.1 Density gradient and viscosity needed to exceed the critical Rayleigh number of 1708 and for natural convection to commence for different characteristic lengths. The last three numbers are omitted since they were so large. 43

5.2 Numerical results obtained for the different scenarios. An effective thermal conductivity is calculated and also the relative thermal conductivity is presented for each melting height and dynamic viscosity. 47

C.1 Specific heat capacity for the high-density polyethylene dependent of temperature. C-1

C.2 Thermal conductivity for the high-density polyethylene dependent of temperature for the HDPE. C-2

C.3 Constant thermal properties for the high-density polyethylene C-2

D.1 Thermal properties for the aluminum and cast iron used in the numerical computations. D-1

Nomenclature

Abbreviations

CAD	Computational-Aided Design
CFD	Computational Fluid Dynamics
HTC	Heat Transfer Coefficient
IWH	Industrial Waste Heat
$LHTES$	Latent Heat Thermal Energy Storage
NTU	Number of Thermal Units
TES	Thermal Energy Storage

Other symbols

α	Thermal diffusivity	$[m^2s^{-1}]$
β	Volumetric thermal expansion coefficient	$[K^{-1}]$
μ	Dynamic viscossity	$[Pas]$
ν	Kinematic viscosity	$[m^2s^{-1}]$
ε	Emissivity	$[-]$
A	Area	$[m^2]$
D	Diameter	$[m]$
D_h	Hydraulic diameter	$[m]$
h	Heat transfer coefficient	$[Wm^{-2}K^{-1}]$
k	Thermal conductivity	$[Wm^{-1}K^{-1}]$
Pe	Perimeter	$[m]$
q	Heat rate	$[W]$
r	Radius	$[m]$
T	Temperature	$[K], [^{\circ}C]$

Physical constants

σ	Stefan Boltzmann constant	$5.67 \cdot 10^{-8} W/(m^2 K^4)$
g	Gravitational constant	$9.81 m/(s^2)$

Subscripts

1	Inner storage surface
2	Exterior storage wall
∞	Ambient/surroundings
c	Cold
ch	Channel
f	Film
fin	Fin
h	Hot
s	Surface

Chapter 1

Introduction

In 2018, the gathered heating and cooling demand in Norwegian households was approximately 37.5 TWh, where 80 % of the need for heating was supplied from electricity [1]. Typically, over 60 % of the total electricity usage in Norwegian households is used for room heating, while approximately 15-20 % of the electricity is used to heat hot tap water [2][3]. Instead of using electricity directly as a heat source, a better way is to exploit heat sources such as wood stoves, waste heat, and heat pumps. Modern wood stoves emit only low emissions of particles and other pollutants and consume only renewable energy sources. Approximately 1.4 million households in Norway use or have the opportunity to use firewood heating. In 2020, Norwegian households and holiday homes used 5.9 TWh energy from wood [4].

The importance of exploiting the energy in the best way is crucial to secure a sustainable and green future. One step on this path has been to mainly build passive houses with sufficiently low demand for heating. As the efficiencies for wood stoves have become better, their nominal duty is typically 5 kW or even more, depending on the firing process. Such heat transfer may lead to overheating the modern houses. As the activity runs out, the drop in temperature adversely provides an unstable heat supply. Due to this, intermediate heat storage for the wood stove may be of interest.

Latent heat thermal energy storage (LHTES), based on heat absorption and release when a storage material undergoes a phase change, is an attractive technology for several applications, including intermediate heat storage in modern wood stoves. LHTES is a way to store thermal energy in an energy-dense way. At the same time, it delivers a more stable heat transfer rate than sensible heat storage since the LHTES manages to hold a more constant temperature due to the phase change. Many phase change materials (PCMs) are well documented in the literature. However, their implementation is still limited due to the complexity of designing a suitable interface between the heat source, PCM, and heat sink.

This master's thesis is a contribution to a project named *IPN PCM-STOVE* which has its aim to even the wood stove's duty and heat delivery by developing a compact LHTES for a wood stove. The thesis builds up on several past master's of science project works where the latest and most complete work was made by Larsen[5]. He built a laboratory pilot of the LHTES, which was based on his calculations and Mathisen's and Lindegård's previous work [6][7]. Preliminary to this thesis, a project work was conducted that investigated the storage's performance based on experimental and numerical calculations. Results indicated that a considerable thermal resistance outside the LHTES hindered a satisfactory heat release.

As a continuation of the already conducted work, this thesis will attempt to reduce the thermal resistance such that the LHTES can reach its deliveries. Another frequent problem for the PCMs suitable for this application is their relatively low degradation temperature. The PCM used in the preliminary work was, in addition, very viscous when melted with low thermal conductivity. Degradation can be a risk when large heat fluxes are obtained from the wood stove. Natural convection could be a passive mixing process that would work as a corrective effect to avoid local overheating.

1.1 Objectives

The purpose is to continue to develop an innovative concept of intermediate thermal energy storage based on PCMs. The following tasks are a copy of this master's thesis scope of work:

1. A literature study on concepts, applications, and technologies using PCMs as intermediate thermal energy storage in industry and buildings shall be conducted.
2. The heat release from the existing PCM storage shall be optimized concerning the desired performance. The focus of this study is on the enhancement of heat transfer between the PCM storage and the heat sink. Performance enhancement methods shall be presented, analyzed, and discussed. Numerical calculations shall be performed to assess the performance of the proposed enhancements.
3. The importance of natural convection effects in heat storage and discharging shall be investigated. Calculations shall be performed on the existing PCM heat storage to evaluate the potential heat transfer enhancement. A discussion on the required PCM properties (principally the liquid phase viscosity) shall be performed.
4. Suggestions for further work shall be made.

1.2 Structure

A short explanation of the report structure and what each chapter will consist of will now be presented. It consists of seven chapters in total. Two different technical studies and themes will be presented in Chapters 4 and 5, representing objectives 2 and 3. The appropriate theory will be presented while the utilized methods are described. Both chapters consist of both conducted estimations and numerical computations. The estimation and numerical sections will each have a subsection presenting the obtained results. A discussion of the methods used and the results presented will follow in its specific chapter. An overview of every chapter and its theme can be seen below.

Chapter 1 is this ongoing introduction where the topic is stated together with the thesis' background and objectives.

Chapter 2 takes upon the first objective, which is a literature study. Different studies using PCMs are briefly presented to enlighten their widespread use.

Chapter 3 is a closer introduction to the project's and report's concept. This introduction will be a more detailed presentation of the LHTES's deliveries and challenges.

Chapter 4 is the first technical chapter that takes on objective number two. The method used to estimate the performance of the enhancement measures is described with the following estimating results. How to obtain more accurately numerically results will be described before the actual computed results are presented. A discussion will be made based on the presented results, followed by a conclusion.

Chapter 5 is the second and last technical chapter in this thesis. It regards objective number three, which concerns how natural convection effects may affect the inner heat transfer. Buoyancy theory, methods used to estimate the onset of natural convection, and results will be presented. Lastly, more detailed and accurate numerical computations are shown, followed by their results. A discussion will follow and is based on the presented results. In the end, a conclusion will be made.

Chapter 6 rounds up everything presented by reproducing each conclusion from Chapters 4 and 5 of the work done.

Chapter 7 is the last chapter and consists of several suggestions for further work.

Chapter 2

Overview of PCM Applications

The usage areas for PCMs are numerous. This chapter will present a few applications with a brief description to show the various application areas. Applications used in the industry, buildings, food industry, and electronic equipment thermal control will be presented.

The different ways of using PCM may be to encapsulate it in a micro or macro-sized container, integrate it in fibers or other materials, or fill up larger containers. The micro-encapsulated PCM is typically 1-300 μm in diameter, while macrocapsules with PCM are capsules with a size usually larger than 1 cm in diameter [8][9]. The temperature range for different PCMs is vast, ranging from -20 °C and up to higher temperatures as 800 °C[10]. The melting temperature has a lot to say about what PCM is utilized in the different applications due to different needs and operating conditions.

2.1 Industrial Applications

There are several ways that PCMs have been used in industrial applications. It may be used in heat exchangers or store excess heat from industrial waste heat (IWH) or other heat generating processes. An example of an experimental study where an LHTES was used to transfer large amounts of excess heat is outlined in the upcoming section.

2.1.1 Application of PCM in Mobilized-Thermal Energy Storage

When there is an absence of nearby heat consumers to an energy source, e.g., IWH, transportable thermal storage can be utilized. These are called mobilized thermal energy storage (M-TES). Deckert et al. performed experiments on a prototype mobile latent heat storage and optimized the charging and discharging processes [11]. The storage consisted of two parallel connected storage tanks which could store up to 2 MWh. The sketch of the tanks from the article is reproduced in Figure 2.1. The storage was transported by a large truck, and the distance needed to travel was 5.6 km. The tanks were filled with salt hydrates as PCM with a melting temperature of 58 °C. The charging temp was set to a constant value equal to 85 °C while the mass flow rate was adjusted. When comparing the heat generation costs of this prototype with other typical heating systems using, i.e., oil and firewood to provide the same heat, the costs were more than halved for the M-TES using PCM.

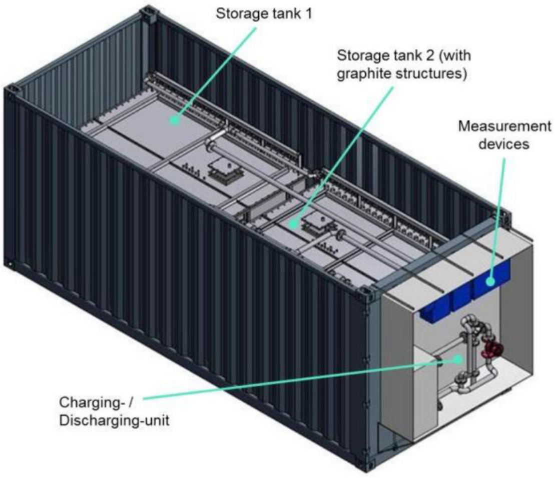
Storage tank 1
Storage tank 2 (with graphite structures)
Measurement devices
Charging- / Discharging-unit

Figure 2.1: This is the sketch of the storage tanks used in the article *"Economic efficiency of mobile latent heat storages"*[11].

2.2 Building Applications

The advantages of implementing an LHTES in buildings may be to reduce the peak demand for electricity and save operating fees and costs. One example is that an LHTES can get charged during the low-peak periods for electricity. Another possibility could be to charge the storage with cold ambient air during the night to be utilized later during the day when it is hotter, instead of using air conditioning based on electricity. Solar energy during the daytime may also be stored and later utilized in buildings during the night to prevent the indoor temperature from falling as low as it usually would have. The LHTES for buildings may both be active and passive methods. Fans can, for instance, be utilized in an active application to force air or another fluid to charge or discharge the storage by convection, or a PCM can be implemented in the building structure, i.e., walls, ceilings, or in the floor as a passive application. Microcapsules with PCM may be integrated inside materials such as concrete to enhance the storage capacity [10]. A PCM may also be implemented under the floor with electrical heating or pipes with domestic heat to increase the heat capacity compared to only using electrical heating, which is the usual way of floor heating. El Mays et al. conducted an experiment using white petroleum jelly as PCM in the under-floor heating together with electrical heating supplied by solar electricity. During the day, electrical heating cords heated the floor simultaneously as they charged the PCM. As the sun went down at night, the charged PCM floor could still provide a comfortable temperature [12]. Another example of a more passive solution will be presented more closely in the upcoming section.

2.2.1 Office Wall Containing PCM for Cooling

Tunçbilek et al. examined the performance of an office wall containing PCM for intermittent cooling operation [13]. The PCM wall worked as a barrier between the solar irradiation and hot outer temperature and the indoor. They investigated how the cooling performance varied for melting temperatures ranging from 20-30 °C, where the aim was for the room temperature to maintain the comfort range of 22-25 °C. The best results were when they used a PCM with a melting temperature of 25 °C. This temperature was the highest set point temperature for the air conditioning. They based their conclusion on how significant the energy savings was by reducing the need for air conditioning during the day. If using a PCM with a lower melting point, a solidification would never occur due to the high outdoor temperature. The PCM worked then as a phase-stabilized material instead. Selecting a PCM with a melting temperature higher than 25 °C would stabilize the walls at a higher temperature than the onset for the air conditioning which would cause the air condition to be activated the whole time.

2.3 Food Applications

Different foods have a large variety of how they need to be treated and stored. Some foods may lose their quality at moderate or high temperatures and must be explicitly stored or processed to obtain a longer shelf life. Two different areas utilizing a PCM to store and process foods are presented.

2.3.1 Food Storing

Cooling elements have been used for a long time already to prevent food from being heated. Other processes and foods may require other properties from a PCM, such as different phase change temperatures. Oró et al. conducted both experimental and numerical investigations on storing ice cream in containers outside a special freezer typically used in kiosks and stores. The idea was to slow the melting process down by exploiting a void around and in between the ice cream containers by filling it with a PCM. The tested PCM had a phase change temperature of -21.3 °C, and the containers were placed outside the specific freezer for three hours. The result showed an overall reduction in the ice cream's temperature rise. The temperature increase in the center and corner was reduced by 3 °C and 10 °C, respectively, when introducing the PCM. This reduced temperature rise ensured a better ice cream quality [14].

2.3.2 Food Processing

An interesting way to exploit a PCM is to conserve foods by drying. This was conducted by Devahastin and Pitaksuriyarat through experimental testing [15]. They used a PCM with a melting temperature range of 35-54 °C and forced convection to dry sweet potatoes. A reproduction of the schematic in the article may be seen in Figure 2.2. The experiments tested how large the energy savings would be by switching from using drying air with an inlet temperature of 60 °C compared to utilizing an LHTES to heat the inlet air from ambient temperature to drying temperatures. The report proved energy savings of 1920 and 1386 kJ/kg when using an inlet air velocity of 1 and 2 m/s, respectively.

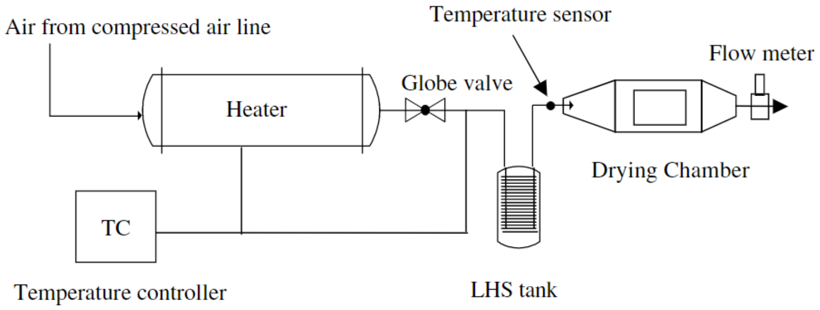

Figure 2.2: This is the schematic diagram shown in the article *"Use of latent heat storage to conserve energy during drying and its effect on drying kinetics of a food product"* of the drying system using a latent heat system[15].

A review on LHTES used in solar drying cabinets for agricultural products has been conducted by Jahromi et al.[16]. The drying process is a time-demanding process that requires a continuously uniform operating temperature. Due to the variations in temperature and solar irradiation during daytime and nighttime, introducing PCM may contribute to an even temperature for a longer time without external energy, which might require electricity to operate. The results conducted in the review were possible energy savings of 2.98-39 % for the solar dryers using PCM compared to the systems without PCM.

2.4 Electronic Chip Applications

Microchips used in electrical components such as computers, mobile devices, and electrical circuit boards are getting smaller, and the number of devices per area increases. The need for thermal control of the chips is therefore increasing. A way of to prevent overheating is through passive cooling using a PCM. A lot of different materials may be suitable for these applications. Examples may be organic, microcapsule, nanomaterials, and composite-PCM [17]. The PCM works as a heat sink, and by placing this near the heat source, a better heat transfer efficiency is obtained. This is due to the lower thermal resistance obtained when the void between the source and sink diminishes. Another way of utilizing PCM in a cooling system is to have a PCM-supported heat pipe that transfers the heat to the main heat sink which was examined by Behi et al. [18]. The next example introduced is the use of PCM for thermal management of a mobile device.

2.4.1 Thermal Management of a Mobile Device

An example of passive thermal management of a mobile device using a PCM may be the work conducted by Tomizawa et al.[19]. They made an experimental and numerical study on the "delay effect" a PCM layer would have on the temperature increase on the heat source itself and on the front case. Results showed that using a PCM layer would delay the temperature rise for both places. However, only a relatively sizeable PCM layer would cause a significant reduction in maximum temperature rise for the heater and the front case. Some sketches from the article is reproduced in Figure 2.3.

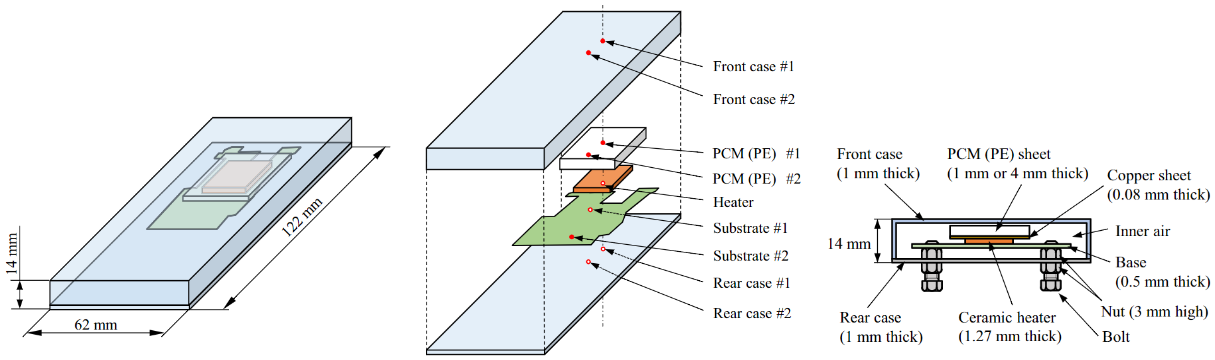
14 mm
62 mm
122 mm
Front case #1
Front case #2
PCM (PE) #1
PCM (PE) #2
Heater
Substrate #1
Substrate #2
Rear case #1
Rear case #2
Front case
(1 mm thick)
PCM (PE) sheet
(1 mm or 4 mm thick)
Copper sheet
(0.08 mm thick)
14 mm
Inner air
Base
(0.5 mm thick)
Nut (3 mm high)
Bolt
Rear case
(1 mm thick)
Ceramic heater
(1.27 mm thick)

Figure 2.3: Sketches of the concept in *"Experimental and numerical study on phase change material (PCM) for thermal management of mobile devices"*[19].

Chapter 3

Concept and Design

Several pieces of research on finding a suitable solution to implement an LHTES together with a wood stove have been conducted prior to this master's thesis. This work was in association with a research and innovation project named *IPN PCM-STOVE*. The goal is to store enough heat to discharge for approximately eight hours with a discharge rate of mainly 500-1000 W. A rough estimate based on these specifications is the desired storage capacity of approximately 6 kWh. A laboratory pilot has already been developed and investigated experimentally and numerically. The full-size storage was supposed to be a 20 cm tall cylinder with a diameter of approximately 50 cm. The pilot is one-quarter of the whole cylinder and half its height. It was filled with a high-density polyethylene (HDPE) working as the PCM with a melting temperature equal to 124.2 °C. Some vertical plate fins were attached to the bottom and side wall to improve the storage's effective thermal conductivity since the HDPE has a small thermal conductivity, which is typical for PCMs. Figure 3.1 pictures a sketch of the concept and the inside of the prototype with the fins placed inside the storage volume. This prototype was built by Larsen during his master's thesis [5].

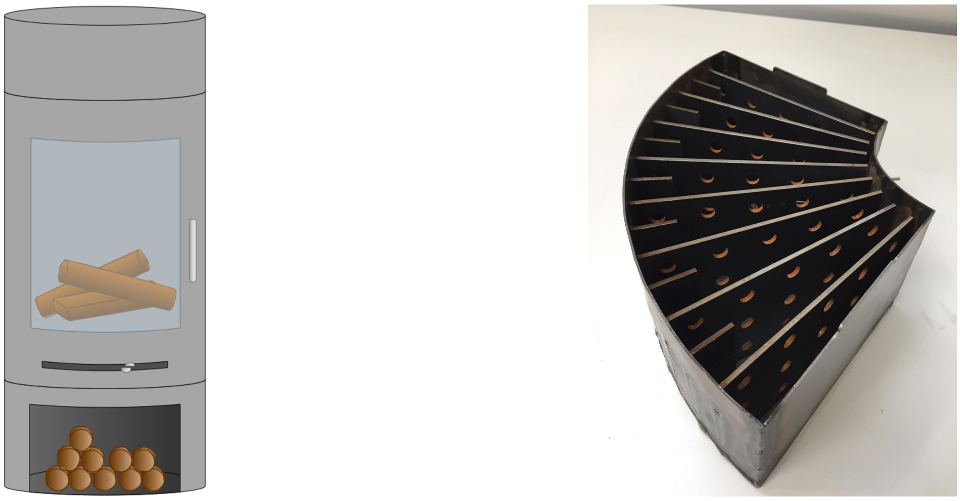

(a) A sketch of a wood stove with an LHTES placed on top.

(b) The container used in the laboratory excluding the lid. This picture was taken by Larsen [5].

Figure 3.1: Sketch of the TES placement and the inside of the exiting laboratory pilot.

A project work was conducted as preliminary work for this master's thesis. This work involved experimental and numerical analysis of the laboratory pilot to establish if the storage could deliver sufficient heat during the desired discharge period. From both the experimental and numerical results, it was clear that the existing storage design was not adequate. The results indicated that the storage reached its lower discharge limit of 500 W after approximately five hours. The storage bulk temperature was almost 100 °C which accounted for a sufficient driving force. A satisfactory temperature at the discharge end is when the storage is at approximately 60 °C. At this temperature, the previous results showed a heat transfer rate of just above 170 W. One part of the conclusion was that the dominant thermal resistance for the heat release was on the outside of the storage volume. A reduced thermal resistance may be obtained by enlarging the outside heat transfer area or the heat transfer coefficient (HTC).

One idea to increase the heat rate at lower storage temperatures was to add an external wall outside the vertical storage wall. By connecting this external wall to the storage with fins holding it together, several channels would be obtained, which would induce a draft of air due to the hot walls. A sketch of the storage with the channels is pictured in Figure 3.2. The idea was for the channels to contribute by enlarging the surface area and to reduce the thermal resistance. The exciting outcome is to assess if the effect of the increased surface and induced channel flow adds up to be beneficial to the total outer heat transfer. In chapter 4, an approach to establish a given number of fins and a slit distance between the inner and outer storage walls, which may provide as high as possible heat release, will be presented. Some assumptions were necessary to assess the eventual benefits of the design modification. These assumptions and approximations will be presented along the way. A given number of fins and a slit distance making the optimal case will be obtained. More detailed CFD computations, with the estimated results as a base, will be executed in Ansys Fluent.

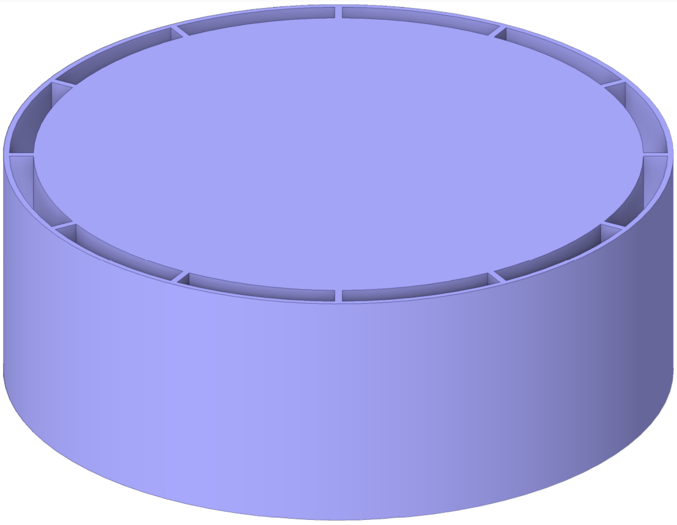

Figure 3.2: Sketch of how the channel arrangement may look like.

Another idea to enhance the outer heat transfer rate was to use the same approach for the channels but to make small tubes going through the storage volume instead. Since the temperature inside the storage center is hotter than further out, more valuable heat from the hot PCM would be utilized. This design would also contribute to enlarging the heat transfer area. One down part about this would be that some of the potential storage capacity would be removed to make room for the tubes.

In addition to the heat transfer challenges outside the storage, investigations of the storage volume's inner heat transfer are also of interest. The low thermal conductivity for the HDPE mentioned earlier is an important issue concerning this LHTES application. It is unclear what heat fluxes may be obtained between the stove and storage. It is, therefore, not assured that the HDPE will not approach its degradation temperature of 300 °C. One approach to reducing the chance of this happening was to attach the fins already introduced. In addition, investigating what effect natural convection in the PCM may have on lowering the danger of reaching 300 °C will be made. Numerical experiments will be executed, and the buoyancy effects on preventing overheating will be analyzed.

Chapter 4

Outer Heat Transfer

Small channels get created when an external wall is connected to the storage by a given number of fins. An induced airflow in the channels, together with the extra surface area introduced, is a design giving promising results for the LHTES's outer heat transfer. The hot exterior surface ensures heat transfer to the room through free convection, q_{conv}, and radiation, q_{rad}. This collected heat transfer can be written as

$$q_{\infty} = q_{rad} + q_{conv} \tag{4.1}$$

where q_{∞} represents the collected heat transfer from this surface. The external wall will also, together with the inner storage surface, transfer heat to the air flowing between these two surfaces, represented as q_{air}. Figure 4.1 illustrates a vertical cross-section of a channel and the outer energy balance for the LHTES. The inner and outer walls hold an average temperature of T_1 and T_2, respectively. Cold ambient air enters the bottom of the channel, gets heated through it, and the hot air exits at the top. The heat released by free convection and radiation from the exterior surface is also pictured as q_{∞}. The heat transfer through the storage top is not included in this sketch.

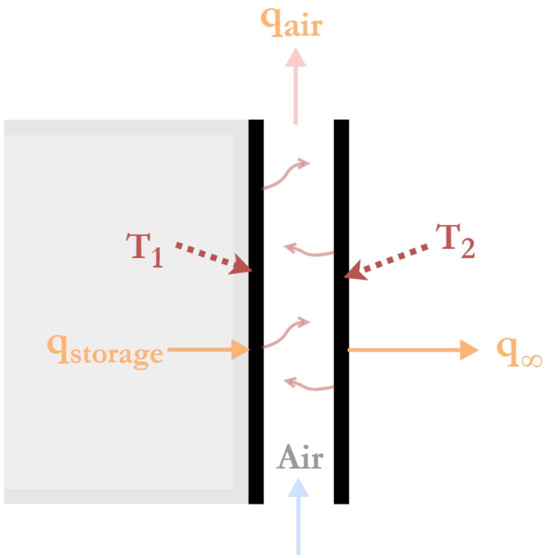

Figure 4.1: Principle sketch of the vertical cross section of one channel obtained between the inner storage surface and the external wall.

$$\frac{dE_{st}}{dt} = \dot{E}_{in} - \dot{E}_{out} = q_{storage} - [q_{\infty} + q_{air}]_{room} = 0 \tag{4.2}$$

It was desired to estimate the outer heat transfer from the LHTES based on these design modifications to see if the TES could close in on its deliveries. When conducting the heat transfer calculations for this design, the system was assumed to be a steady-state problem following the energy balance in Equation (4.2). The outer heat transfer could then be analyzed for different operating conditions and arrangements consisting of a different number of fins and slit distances. The slit distance equaled the fins' lengths and was the distance between the inner and outer channel wall. The different operating conditions were different constant inner surface temperatures (T_1) and different thermal conductivities for the storage container. Further, an optimal number of fins and a given slit distance will be obtained based on what arrangement supplies the highest heat release. The following sections will walk through what assumptions and methods were made and used to perform these design estimations. The "optimal" design was investigated closer in detail using computational software. These results are presented later in the chapter.

4.1 Estimating an Optimum Channel Arrangement

This section will present the approach used to estimate an optimum arrangement of number of fins and slit distance. The present heat transfer contributions will be introduced, including how these may be accounted for in the computations. In the end, the estimated optimum arrangement will be presented together with some performance numbers.

4.1.1 Radiation

Due to hot outer storage surfaces, radiation plays a part in the total outer heat transfer as displayed in Equation (4.1). Its extent depends on the material's surface emissivity and the surface and surrounding temperatures. The heat rate caused by radiation is given as

$$q_{rad} = \varepsilon \sigma A_s (T_s^4 - T_{\infty}^4) \tag{4.3}$$

An HTC, h_{rad}, can be derived and represent the heat transfer in a way that will be preferable later when summing up the radiation and free convection contributions. Rearranging Equation (4.3), a radiative HTC is expressed as

$$h_{rad} = \varepsilon \sigma (T_s + T_{surr})(T_s^2 + T_{surr}^2) \tag{4.4}$$

where temperatures are given in Kelvin, ε is the emissivity, and σ is Stefan-Boltzmann's constant. This expression implies that h_{rad} is a function of temperature. Equation (4.3) can then be written as

$$q_{rad} = h_{rad} A_s (T_s - T_{\infty}) \tag{4.5}$$

An expression representing the radiative HTC as a function of surface temperature and emissivity could be derived from Equation (4.4). This expression was used later in the estimating and numerical computations.

4.1.2 Natural Convection on External Surfaces

When cold ambient air flows across or along a hot surface, buoyancy forces occur due to the air getting heated and leading to density changes. The hot air adjoining the surface will rise, and the colder air falls downwards, creating upward air motions which causing natural convection. The TES consists of horizontal and vertical surfaces exposed to ambient air, which means natural convection occurs on two different surface orientations. Two different HTCs are required to estimate the heat transfer rate from the surfaces due to natural convection. These coefficients are found from empirical correlations, considering the fluid's properties and flow regime. A dimensionless parameter that tells something about the buoyancy flow regime is the Rayleigh number, Ra, and is expressed as

$$Ra_L = \frac{g\beta(T_s - T_\infty)L_C^3}{\nu\alpha} \tag{4.6}$$

The Rayleigh number characterizes the fluid's flow regime in the same way as the Reynolds number, but it is associated with buoyancy-driven flows instead of forced flow. The fluid's Rayleigh number and Prandtl number, Pr, are used in empirical models to estimate a Nusselt number, Nu. The Nusselt number is a dimensionless way to express the convective HTC. A suiting HTC, h_{conv}, is found to be used in *Newton's law of cooling* which is reproduced in Equation (4.7).

$$q_{conv} = h_{conv}A_s(T_s - T_\infty) \tag{4.7}$$

For simplicity, a total HTC may be obtained from Equation (4.1) where the total heat transfer coefficient is given as $h_\infty = h_{rad} + h_{conv}$. Since both the radiative and convective HTCs depend on temperature, h_∞ is also a function of temperature. As for the radiative HTC, a temperature-dependent HTC representing free convection can also be derived. How to obtain these expressions will be presented below, and the expressions can be viewed in Appendix B.

The empirical models used to find a flow's Nusselt number can, for instance, be found in the book *Fundamentals of Heat and Mass Transfer*[20]. The flow proved to be in the laminar region in the pertinent temperature range at both the horizontal and vertical surfaces.

Buoyancy Driven Flow on Horizontal Plate

A suitable expression to calculate the Nusselt number for the top surface of the storage was Equation (4.8). The Prandtl number is preferred to be larger than or approximately equal to 0.7 to use this expression. Air at 20-230 °C has a Prandtl number ranging between 0.684 and 0.707, which was assumed acceptable.

$$\overline{Nu}_L = 0.54 Ra_L^{1/4} = \frac{\overline{h}_{conv} L_C}{k} \tag{4.8}$$

The characteristic length is given as $L_C = \frac{A_s}{Pe}$ where A_s is the surface area, and Pe is the perimeter of the surface. k is the thermal conductivity of the fluid. Both Rayleigh number and k were obtained at film temperature of the air adjacent to the surfaces, $T_f = (T_s + T_\infty)/2$.

Buoyancy Driven Flow on Vertical Plate

Equation (4.9) was used to find an HTC for the vertical surface of the storage. This expression is mainly derived for a vertical flat plate but is also applicable for vertical cylinders with a height L and diameter D if $\frac{D}{L} \geq \frac{35}{Gr_L^{1/4}}$. The fluid properties are represented at film temperature, T_f, as they were for the horizontal expression.

$$\overline{Nu}_L = 0.68 + \frac{0.670 Ra_L^{1/4}}{[1 + (0.492/Pr)^{9/16}]^{4/9}} = \frac{\overline{h}_{conv} L_c}{k} \tag{4.9}$$

The Grashof number (Gr) is a dimensionless number that is a measure of the ratio between buoyancy and viscous forces [20] and can be calculated from

$$Gr = \frac{g\beta(T_s - T_\infty)L^3}{\nu^2} = \frac{Ra}{Pr} \tag{4.10}$$

4.1.3 Convective Heat Transfer Inside a Channel

Parallels may be drawn to forced convection and air draft through chimneys when estimating the heat transferred to the cold air flowing through the storage's channels. A series of approximations and assumptions were considered for the calculations. First, the airflow was assumed to be fully developed. In retrospect, this assumption proved to be insufficient as neither the hydrodynamic nor the thermal entry length was reached during the entire channel. By assuming fully developed flow, the velocity and flow regime were estimated, and an appropriate HTC in the channel, h_{ch}, could be obtained.

Further, the channel wall temperature was needed to determine the outlet air temperature. The heat transferred through the channel could be calculated by obtaining these values. The external wall was assumed to only get its heat through conduction through the fin and not radiation from the inner surface, even though a temperature difference would be present.

The pressure drop through one channel was assumed to correspond to friction losses to carry out an average velocity. The pressure loss, ΔP, for the air through the channel was given as

$$\Delta P = \Delta \rho g L \tag{4.11}$$

where L is the length of channel, and $\Delta\rho$ is the density change through the channel. It was the density changes that counted as the driving forces. For fully developed flow in a pipe, friction losses are given as

$$F = f_D \frac{\rho}{2} \frac{v^2}{D_h} L \tag{4.12}$$

where the hydraulic diameter is $D_h = 4A_c/Pe$. A_c is the cross-section of the channel, and Pe is the "wetted" perimeter. The friction factor, f_D, depends on the channel's geometry and boundary conditions. In this particular case, the surface temperature for the channel was assumed to be uniform even though the outer and inner channel wall temperatures would differ slightly. For simplicity, the channels in this report were approximated to rectangular ducts even though they were somewhat curved. Different aspect ratios for rectangular ducts correspond to different friction factors and Nusselt numbers. Since the channels' aspect ratio varied depending on the number of fins and slit distance, a linear interpolation between aspect ratios was assumed to hold a good enough approximation for the different cases. The aspect ratios considered, together with the corresponding friction factors and Nusselt numbers, are tabulated in Table 4.1. The aspect ratio is the relationship between the average inner and outer channel wall, b, and the slit distance, a.

Aspect ratio $\left(\frac{b}{a}\right)$	**Re/f$_\mathbf{D}$**	**Nu=(hD$_h$)/k**
1.0	57	2.98
1.43	59	3.08
2.0	62	3.39
3.0	69	3.96
4.0	73	4.44
8.0	82	5.60
∞	96	7.54

Table 4.1: Friction factor and Nusselt number for different aspect ratios for a rectangula duct. The aspect ratio is the ratio between the average of inner and outer channel wall, b, and the slit distance, a. These tabulated numbers apply for uniform surface temperatures and for a laminar and fully developed flow.

An average velocity was determined from Equation (4.11) and Equation (4.12), which further proved the airflow to be in the laminar region. An appropriate Nusselt number was obtained by linear interpolation from Table 4.1 depending on the channel dimension. An HTC for the channel flow was obtained from the Nusselt number and will be referred to as h_{ch}. This HTC would then be used to estimate the channel wall temperature and later the outlet temperature. A fin approximation was used to calculate an appropriate channel wall temperature. For the outlet temperature, a method called the effectiveness-NTU method was used, which is a method made to estimate the design and performance for heat exchangers. These two approaches are presented next.

Fin approximations

An appropriate channel wall temperature, T_{ch}, was assumed to be represented by the average between T_1 and T_2. A fin approach was used to find the external wall temperature, T_2. Figure 4.2 illustrates the top view of the channels where T_1 represented the temperature for the inner storage wall, S was the slit distance, and L was half of the outer channel wall.

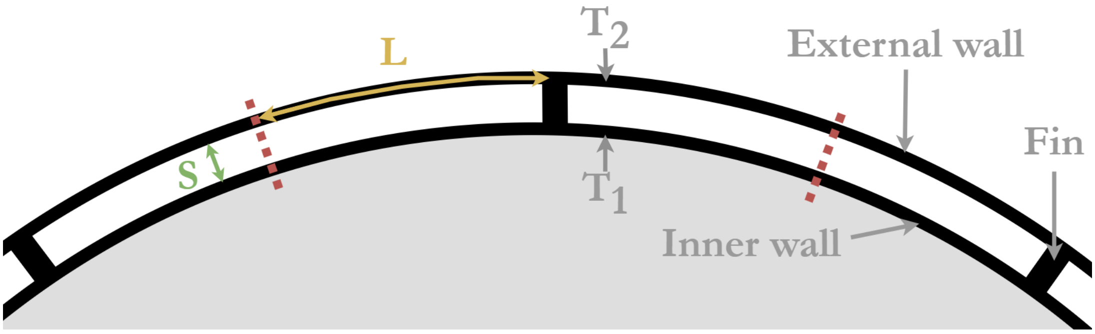

Figure 4.2: Sketch of the top view of channels obtained between the inner and external storage walls.

To perform the calculations on the external wall temperature, T_2, the outer channel wall was divided in half and extended into a long fin normal to the storage surface as shown in Figure 4.3. In reality, there were two different HTCs surrounding the fin. One on the outside and one on the inside of the fin, h_∞ and h_{ch}, respectively. An average of the HTCs obtained inside and outside the channel was used in the fin approximations. This HTC will be referred to as $h_{fin} = (h_{ch} + h_\infty)/2$.

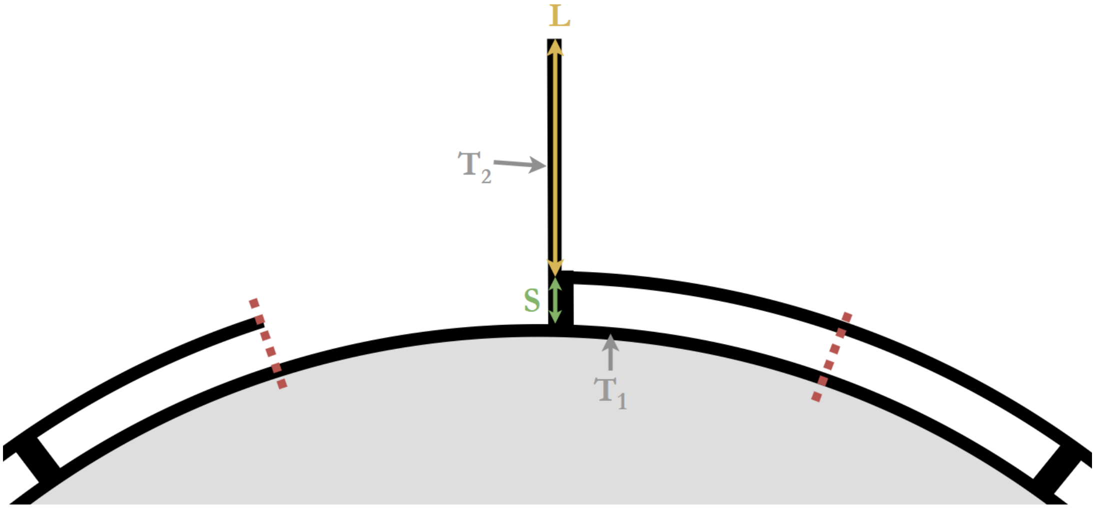

Figure 4.3: Sketch of the fin approach for calculating the temperature distribution in the external wall.

The fin tip was assumed adiabatic due to symmetry. For a fin with an adiabatic tip, the heat transfer rate conducted through the fin was given as

$$q_f = \sqrt{h_{fin} P k_{fin} A_c}\,\theta_b \tag{4.13}$$

where P is the perimeter, A_c is the cross-section of the fin and $\theta_b = T_b - T_\infty$. T_b is the fin base temperature and was, in this case, equal to the inner surface temperature, T_1. The fin's thermal conductivity, k_{fin}, affects such as the fin temperature. A higher conductivity may lead to a higher heat transfer through the fin and a smaller temperature drop.

The fin efficiency, η_{fin}, for an adiabatic fin tip is given as

$$\eta_{fin} = \frac{tanh(mL)}{mL} \tag{4.14}$$

but is also said to be equal the ratio between the heat rate conducted through the fin, q_{fin}, and the maximum driving potential for the convection, q_{max}, shown in Equation (4.15).

$$\eta_f = \frac{q_f}{q_{max}} \tag{4.15}$$

The maximum driving potential is the heat transfer rate obtained if the whole fin surface area, A_f, is said to be at the base temperature. Equation (4.15) was, together with Equation (4.14), used to estimate an average fin temperature representing the external wall temperature, T_2. First, the fin efficiency could be calculated by Equation (4.14). Second, an approximation of Equation (4.13) was written as

$$q_f = h_{fin} A_f (T_2 - T_\infty) \tag{4.16}$$

By substituting Equation (4.14) and Equation (4.16) into Equation (4.15), the average fin temperature was estimated by

$$T_2 = \eta_f (T_b - T_\infty) + T_\infty \tag{4.17}$$

At last, the average channel wall temperature, T_{ch}, was set to the average of T_1 and T_2.

The Effectiveness-NTU method

When the size of a heat exchanger is known, one can estimate the performance by using the ε-NTU method. First, the number of thermal units (NTU) is calculated from Equation (4.18). This number is then used to estimate the heat exchanger's effectiveness, ε. This approach will be accounted for the heat exchange between the channel wall and air.

$$NTU = \frac{h_{ch} A_s}{\dot{m} c_p} \tag{4.18}$$

In Equation (4.18), h_{ch} corresponds to the HTC estimated for the airflow through the channels due to buoyancy effects. A_s is the channel surface area where heat exchange happens, $\dot{m}$ is the mass flow of air flowing through one channel, and c_p is the air's mean specific heat capacity.

The maximum heat transfer possible from the channel surface to the working fluid in the channel is $q_{max} = C_{min}(T_{ch} - T_\infty)$ where C_{min} is the smallest heat capacity rate out of the "hot" (h) and "cold" (c) side. Actual heat transferred to the cold air is given as

$q_{air} = C_c(T_{out} - T_\infty)$ where T_{out} is the air temperature when exiting the hot channel. The ratio between actual and maximum heat transfer is the heat exchange effectiveness (ε). The effectiveness is given as Equation (4.19) and can, together with the calculated NTU, be used to estimate T_{out}.

$$\varepsilon = \frac{q}{q_{max}} = \frac{C_c}{C_{min}} \frac{T_{out} - T_\infty}{T_{ch} - T_\infty} = 1 - exp(-NTU) \tag{4.19}$$

Since the hot channel walls were assumed to hold a constant temperature, T_{ch}, compared to the temperature change for the cold air, the heat capacity rate for the hot side, C_h, was said to be much larger than the cold side ($C_h >> C_c$). Therefore, $C_{min} = C_c$, and the temperature of the air flowing out of the channel could easily be calculated as

$$T_{out} = \varepsilon(T_{ch} - T_\infty) + T_\infty \tag{4.20}$$

and the amount of heat transferred to the channel air was found.

4.1.4 Resulting Channel Arrangement

This section presents the estimated total heat release from channels obtained for a different number of fins and different slit distances. The results will be commented on briefly, and a more comprehensive discussion is done in Section 4.5.

The previous sections went through how the hot storage surfaces participate in the storage's heat transfer process and how the external wall temperature was approximated. Based on these earlier equations, an optimal number of fins and slit distance would be obtained based on the arrangement providing the most significant heat release. The end of the discharge period was, as mentioned, said to be when the storage bulk temperature is 60 °C. Due to the desire to enhance the discharge power at the discharge end, this was where the optimum estimate mainly was of interest. The calculations of the outer heat transfer were conducted for two different thermal conductivities. In this way, the benefits of choosing different container materials could be evaluated. The conductivities investigated were 50 and 200 W/(mK), representing cast iron and aluminum. Their emissivity was both set to 0.8, assuming the aluminum was anodized. These properties were simplified to be independent of temperature both in the estimations and the more thoroughly numerical computations later.

In Figure 4.4, the total heat transfer rate from the full-size storage is pictured as a function of slit distance. Each graph in the figure represents a different number of fins. A range from 8 to 18 fins was examined. The peak of each curve in Figure 4.4 is reproduced in Table 4.2 and Table 4.3 for the cast iron container and aluminum container respectively. The overall surface efficiency for each peak is also included in the tables as η_0. This tells how good the extended surface is working. An overall surface efficiency of 100 % is the case if the whole extended surface is equal to the hot base temperature.

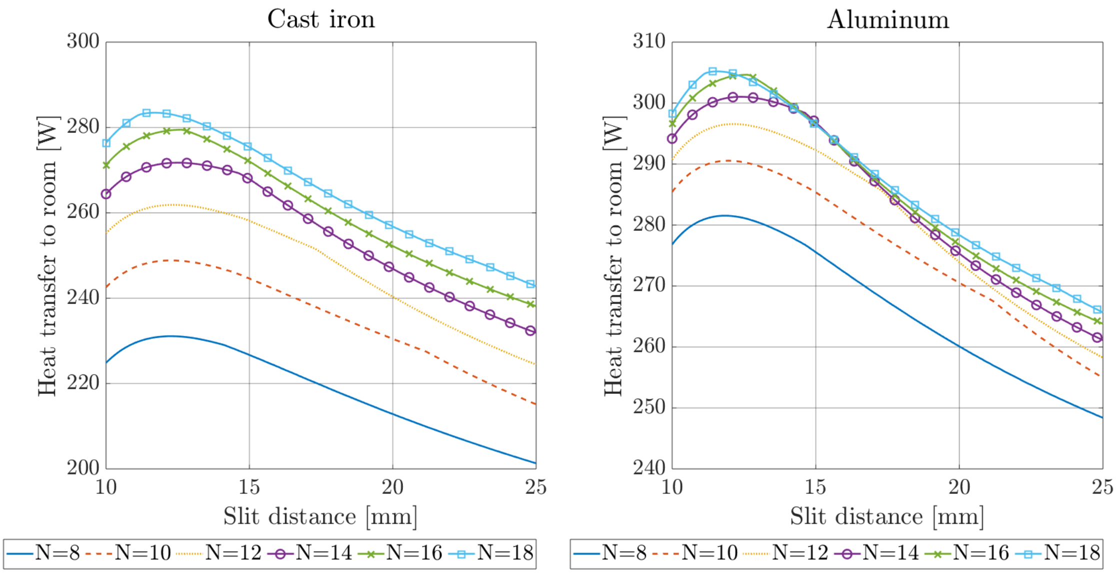

Figure 4.4: Estimated total heat transfer from the LHTES when the inner surface holds a uniform temperature of 60 °C. The different graphs represents different number of fins (N).

Cast iron (T_1=60°C)	**8 fins**	**10 fins**	**12 fins**	**14 fins**	**16 fins**	**18 fins**
Total heat rate [W]	231.1	248.8	261.9	271.7	279.5	283.5
Heat rate increase	-	7.7 %	5.2 %	3.8 %	2.9 %	1.4 %
Slit distance [mm]	12.2	12.2	12.3	12.5	12.6	11.7
η_0	77.8 %	82.7 %	86.1 %	88.5 %	90.3 %	91.7 %
Weight increase	-	0.2 %	0.8 %	1.4 %	0.8 %	-4.9 %

Table 4.2: Summary of estimations for a cast iron container at 60 °C. The peak of heat transfer curve for each number of fins are reproduced.

Aluminum (T_1=60°C)	**8 fins**	**10 fins**	**12 fins**	**14 fins**	**16 fins**	**18 fins**
Total heat rate [W]	281.5	290.5	296.6	301.0	304.7	305.2
Heat rate increase	-	3.2 %	2.1 %	1.5 %	1.2 %	0.2 %
Slit distance [mm]	11.8	11.9	12.1	12.4	12.6	11.6
η_0	92.0 %	94.3 %	95.7 %	96.6 %	97.2 %	97.7 %
Weight increase	-	0.8 %	1.4 %	2.0 %	1.4 %	-5.4 %

Table 4.3: Summary of estimations for an aluminum container at 60 °C. The peak of heat transfer curve for each number of fins are reproduced.

To evaluate which arrangement would be the best one for each material, the increase in heat rate was of interest, but the change in container weight may also be considered. Questions assessed were: ”when was the heat rate gain insignificant, and how did the size and weight of the container change?” In Table 4.2 and Table 4.3, the margin in both heat transfer and weight were presented for each case when adding two more fins. The heat transfer gain was evaluate to be insignificant beyond 16 fins for both the cast iron and aluminum containers.

The decrease margin in heat rate may be explain by the decreasing in aspect ratio as fins are added. Both an increase in slit distance and the number of fins lead to a decrease in the channel's aspect ratio. This decrease indicates a decrease in the Nusselt number. The hydraulic diameter and the Nusselt number are proportional to each other. Even though the hydraulic diameter also decreases when adding more fins, the decrease in Nusselt number seems to outweighs the decrease in D_h and the HTC in the channel decreases.

Due to some rough approximations, the optimum slit distance in Figure 4.4 was assessed to take place somewhere between 11 and 14 mm for all numbers of fins checked. There were some uncertainties around these results due to the different approximations, such as neglecting the radiation contribution from surface 1 to 2 and assuming fully developed flow. An optimum arrangement was, from the results, assessed to be 16 fins and a 13 mm slit distance. 18 fins may have been better for cast iron, but one equal geometry was chosen for simplicity. This arrangement was obtained for both cast iron and aluminum. A more comprehensive computation of this geometry was done using numerical computations.

The obtained enhancement in heat release when implementing channels was concluded to be promising. An estimated heat transfer from the storage top was based on previous experimental data and set to be almost 32 W. An estimated heat transfer rate for the full-size storage may be obtained by adding the estimated duty from the top and the 16 channels. The cast iron and aluminum container was estimated to supply a total of 278.7 W and 303.7 W, respectively. These results apply when the inner storage wall measures 60°C. Comparing these numbers with the estimated heat transfer of 171W from the original TES design, an increase in heat release performance would be 63 % if the storage was made out of cast iron and 78 % if switching to aluminum. More detailed and comprehensive computations were done in Ansys Fluent and will be presented in Section 4.3.

For curiosity, if the inner storage surface was 200 °C and the storage consisted of 16 fins and the same slit distance, the estimated heat rate was calculated to be 1 796 W and 2 034 W for a cast iron and aluminum container, respectively. Some of the results may be seen in Table 4.4.

Heat transfer estimates for T_1=200°C	**Steel**	**Aluminum**
Slit distance [mm]	13	13
Number of fins	16	16
Total heat rate [W]	1 796	2 034
Temperature external wall [°C]	168	190
η_0	87.5 %	96.1 %

Table 4.4: This summarizes the most important results for the estimated heat transfer when the inner storage surface holds 200 °C.

The enhancement in outer heat transfer would lead to a decrease in discharge duration.

4.2 Investigating Effects from Tubes Through the Storage

Another approach to enhance the outer heat transfer was to implement small tubes going through the storage. The same approach was used to evaluate the possible benefits.

The estimated gain from one tube with a diameter of 1 cm was just above 1 W if the tube held a surface temperature of 70 °C. The tube wall temperature was higher than the outer wall, which would maybe be 60 °C simultaneously since the storage center would hold a higher temperature. Placing several of these tubes inside the storage would increase total heat release. Increasing the tube diameter would lead to a more considerable gain but would, at the same time, be at the expense of valuable storing capacity.

Since the gain was considered minor, and the tubes displacing valuable PCM volume, this design was chosen not to be carried further.

4.3 Numerical Computation on Channel Flow

Since the already obtained heat transfer estimates were results from many different assumptions and approximations, the performance of the cast iron and aluminum channels was computed numerically to obtain more accurate numbers. To perform numerical computations, the software Ansys Fluent was exploited. In Ansys Fluent, there are two methods to simulate natural convection and buoyancy-driven flows. One way is to perform a transient method, and the other is to perform a steady-state calculation using the *Boussinesq model.* The latter method is described closer in the Ansys Fluent theory guide [21]. The transient method is for large temperature differences in the domain, while the steady-state method is for systems with small temperature differences. A large temperature difference is obtained when the TES is fully charged. Therefore, the transient method was used. The method used in this report to simulate the buoyancy-driven flow through the channel will be briefly outlined, while a more detailed description can be found in the software's Theory Guide [22].

4.3.1 Geometry and Meshing

Since the optimal arrangement of a cast iron container and aluminum container consisted of the same number of fins and the same slit distance, one CAD model was made and used when computing both containers' performance. The model represented one out of the 16 channels in total with a slit distance of 13 mm and side walls representing symmetry. This approach was to minimize the computation time. The CAD model is pictured in Figure 4.5.

The proximity mesh was used to register the details and curvature of the channels. When computing natural convection, a fine enough surface mesh is essential to get the correct behavior of the velocity and shear stresses along the wall.

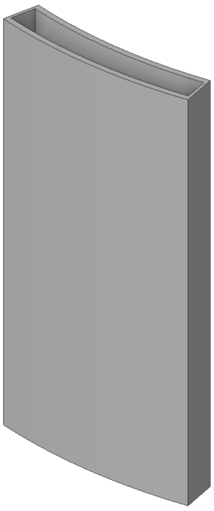

Figure 4.5: CAD-model representing one out of 16 channels constituting the vertical storage wall.

Mesh Independence Study

A mesh independence study was conducted to obtain a mesh with enough cells for the computations. The average velocity out of the channel was analyzed together with the heat transfer out of the channel. The mesh was refined until the outputs converged. The converged solutions can be seen in Figure 4.6 as a function of the number of cells.

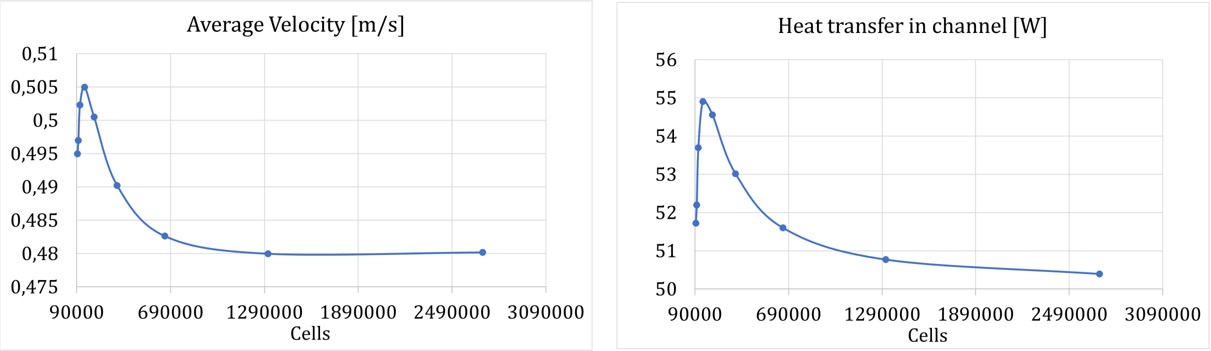

(a) Mesh independence study of average velocity out of the channel.

(b) Mesh independence study of the heat transfer in the channel.

Figure 4.6: Graphs from the mesh independence study conducted on the channel flow.

In addition, to make sure the mesh held a certain quality, *maximum skewness* and *minimum orthogonal quality* were two parameters said to be satisfying if they were less than 0.7 and higher than 0.1, respectively. The resulting mesh consisted of 1 313 446 cells in total. A closeup of the volume mesh is pictured in Figure 4.7.

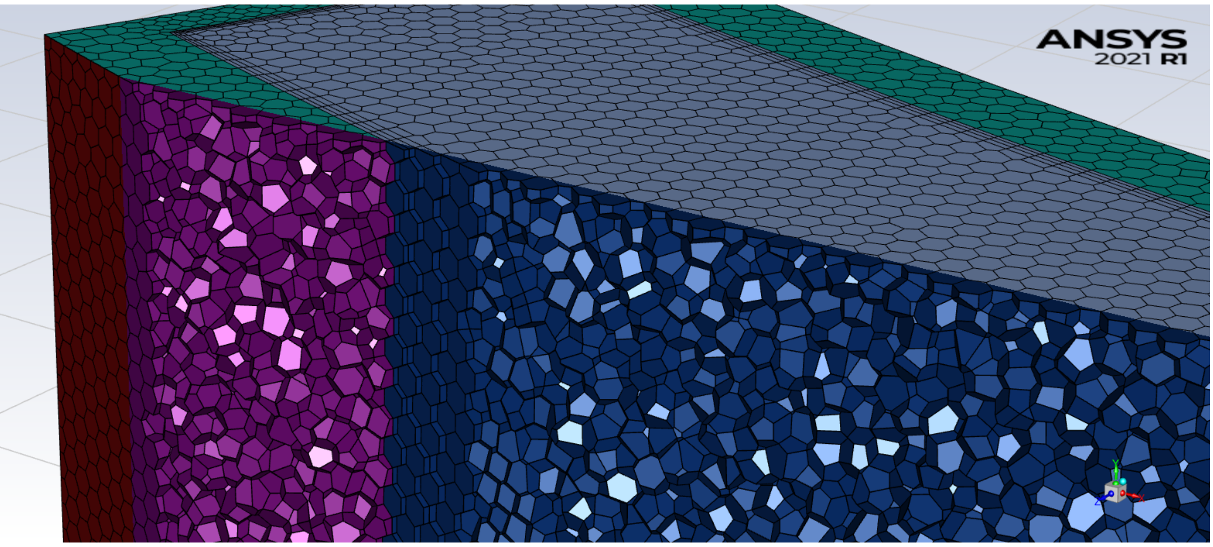

Figure 4.7: Close up on the volume mesh generated for the channel calculations.

4.3.2 Models

When the transient model for buoyancy-driven flow was prepared, such as the *Specified Operating Density* was enabled in the operating conditions. A suitable value for the operating density was the density for air at inlet temperature. A temperature-dependent air density was entered as a piece-wise linear function from tabulated properties at atmospheric pressure. The *Pressure-velocity Coupling Scheme* was set to PISO as this was recommended for transient calculations. This scheme reduces the importance of using small time steps while running the simulation. Buoyancy-driven flows were also recommended to use PRESTO! as the *Spatial Discretization Method* for pressure. The flow regime was earlier found to be within the laminar region, and therefore, the viscous model was set to laminar.

It was conducted computations both when neglecting and including radiation to watch which effects radiation would have on the total heat transfer. *Discrete Ordinates* (DO) was chosen for the radiation computations. The properties of the different materials used for the channels may be found in Appendix D

4.3.3 Boundary Conditions

When simulating a buoyancy-driven flow, the inlet and outlet boundaries were set to pressure-inlet and -outlet, where they both were set to zero gauge pressure. An absolute temperature of 293.15 K at the inlet was entered to represent the cold ambient air in the room. Also, when including radiation, the *External Black Body Temperature Method* for the inlet was kept as default (Boundary Temperature). At the same time, the outlet was changed to Specified External Temperature, which was set to 293.15 K. This way, the radiation out of the inlet and outlet would be included.

In total, four cases were computed. Two of them were for the inner storage wall holding 60

°C and the two others when holding 200 °C. The performance of cast iron and aluminum channels was computed at both temperatures. The inner channel wall was set to hold a constant temperature equal to one of the two mentioned. The outer surface was set to *convection* where a temperature-dependent expression for an HTC was entered. This HTC represented radiation and free convection at a vertical plate. This expression was a function of wall temperature and can be found in Appendix B. The boundaries' internal emissivity was set to 0.8 for the inner channel surface when including radiation. The exterior surface's internal emissivity was set to zero since the radiative contribution was already included in the expression for the HTC. The air properties added due to radiation were kept as default, while the aluminum's and cast iron's absorption coefficient was set to 0.8. The scattering coefficients were held as zero. The diffuse fractions for the walls were also kept as default.

4.3.4 Numerical Results

Results of the four different cases when neglecting and including radiation will be presented in the next sections. Two of the cases were for a cast iron channel and the two others were for aluminum. The two different cases for each material were with a constant inner surface temperature of 60 °C and 200 °C.

Without Radiation

The most interesting outputs from each case is reproduced in Table 4.5 and Table 4.6 for storage surface temperatures of 60 °C and 200 °C respectively. Both estimated and numerical results are presented together in these tables. The heat and mass flow rates given in the tables represent one out of the 16 channels. The heat transfer rates are for only one of the 16 channels and do not include the heat from the storage top.

Storage at 60 °C	**Estimated results**	**Numerical results**	**Deviation**
Cast iron			
Heat Transfer Exterior [W]	7.8	7.0	-10.3 %
Heat Transfer Channel [W]	7.7	8.0	3.9 %
Sum Heat Transfer [W]	15.5	15.0	-3.2 %
Mass flow [g/s]	0.41	0.32	-22.0 %
Aluminum			
Heat Transfer Exterior [W]	8.9	8.6	-3.4 %
Heat Transfer Channel [W]	8.1	8.8	8.6 %
Sum Heat Transfer [W]	17.0	17.4	2.4 %
Mass flow [g/s]	0.42	0.33	-21.4 &

Table 4.5: Estimated and numerical results of the channel performance when the inner surface hold a temperature of 60 °C.

The results show that the channels enhance the outer heat release at lower storage temperatures than the original design. Even though there are some deviations between the

Storage at 200 °C	**Estimated results**	**Numerical results**	**Deviation**
Cast iron			
Heat Transfer Exterior [W]	51.4	43.1	-16.1 %
Heat Transfer Channel [W]	41.2	45.4	10.2 %
Sum Heat Transfer [W]	92.6	88.5	-4.4 %
Mass flow [g/s]	0.84	0.55	-34.5 %
Aluminum			
Heat Transfer Exterior [W]	63.1	59.4	-5.9 %
Heat Transfer Channel [W]	44.3	50.8	14.7 %
Sum Heat Transfer [W]	107.4	110.2	2.6 %
Mass flow [g/s]	0.86	0.57	-33.7 %

Table 4.6: Estimated and numerical results of the channel performance when the inner surface hold a temperature of 200 °C.

estimated and numerical computed results, the total heat transfer from the wall and channel is not that different comparing the estimated and numerical results. The contribution of attaching the external wall with fins almost doubles the heat transfer rate compared to the heat release from the original vertical storage wall. When including the estimated heat loss from the storage top in the numerical results, the storage's total outer heat transfer rate at 60 °C would be 271.7 W and 310.1 W for cast iron and aluminum, respectively. This amount to 58 % and 80 % gain compared to the original 171 W due to the design modifications.

The numerical results imply a lower total heat transfer for cast iron than the estimated duty. For the aluminum channel, the numerical total heat release is larger than the estimated. A closer comment on these results will be made in Section 4.5.

Including Radiation

The heat transfer from the vertical storage wall and channels when including radiation is presented in Table 4.7 and Table 4.8 for inner storage surface temperature of 60 °C and 200 °C, respectively.

The results show that the contribution from radiation is most significant when the channels consist of cast iron. Due to its lower thermal conductivity, a higher temperature gradient will occur between the inner and outer channel surfaces. Therefore, the cast iron has more radiative potential than the aluminum channels.

It will be natural for the modified storage to discharge faster than today's existing design due to the enhanced heat release. Two different computations of the discharge process were conducted and are presented in the next section. One case was the discharging of the LHTES without channels, and the other one was for the storage with channels. Even though the increase in heat transfer for the aluminum channel at 200 °C was substantial when including radiation, the discharge simulation with channels was conducted without enabling radiation due to demanding computation and the increase in required running time following.

Storage at 60 °C	**Numerical results with radiation**	**Improvement when including radiation**
Cast iron		
Heat transfer Exterior [W]	7.2	2.2 %
Heat transfer Channel [W]	8.5	6.2 %
Sum Heat Transfer [W]	15.7	4.6 %
Mass flow [g/s]	0.32	0.4 %
Aluminum		
Heat transfer Exterior [W]	8.6	0.1 %
Heat transfer Channel [W]	8.9	1.5 %
Sum Heat Transfer [W]	17.5	0.8 %
Mass flow [g/s]	0.33	0.6 %

Table 4.7: Numerical results when including radiation in the channel computations when the inner surface hold a temperature of 60 °C. The change in results by including radiation compared to neglecting it is also presented.

Storage at 200 °C	**Numerical results with radiation**	**Improvement when including radiation**
Cast iron		
Heat transfer Exterior [W]	45.6	5.5 %
Heat transfer Channel [W]	49.6	8.5%
Sum Heat Transfer [W]	95.2	7.6%
Mass flow [g/s]	0.55	0.6%
Aluminum		
Heat transfer Exterior [W]	59.9	0.7 %
Heat transfer Channel [W]	55.5	8.5 %
Sum Heat Transfer [W]	115.4	4.6 %
Mass flow [g/s]	0.57	0.1 %

Table 4.8: Numerical results when including radiation in the channel computations when the inner surface hold a temperature of 200 °C. The change in results by including radiation compared to neglecting it is also presented.

4.4 Change in Discharge Period

Two transient discharge simulations were executed to demonstrate the enhanced discharge effects obtained for the LHTES with channels. One simulation represented the plain cylindrical container, and the other one with channels attached to the cylinder's outer wall. Since the aluminum channels achieved a more favorable heat rate than the cast iron channels, it was decided to conduct the discharge computation with aluminum channels. The main container was still cast iron, while the fins and external wall attached were made out of aluminum. Pictures of the two CAD models can be seen in Figure 4.8. These models represented a one-sixteenth part of the whole storage. A small volume at the top of the container volume can be observed in the figures. This void is a 1 cm tall air volume present as a precaution due to volume expansion when the HDPE is heated.

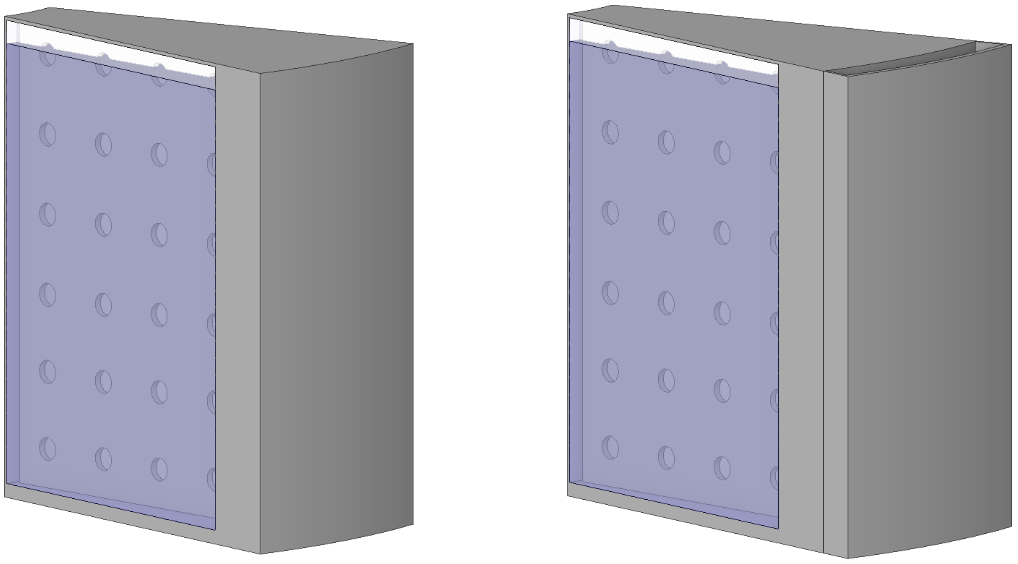

(a) Storage without channels. (b) Storage including channels.

Figure 4.8: The two CAD models used to compute the discharge process for the LHTES without and with channels.

4.4.1 Method

The storage's initial condition for the discharge period was set to a uniform temperature equal 190 °C. When a PCM temperature of 60 °C represents the end of the discharge period, the storage would then be fully charged. The container would contribute with 0.8 kWh, while the PCM volume stored 5.2 kWh, giving a total amount of stored energy of 6 kWh. The energy stored in the container is without considering the channels. These contribute to some more stored heat. This total amount of energy equals the estimated charging capacity desired. Even though the uniform initial temperature might not be a realistic initial state, it was assumed to ease the numerical simulations.

Thermal Properties

From the preliminary project work and Larsen's master's thesis [5], thermal properties for the HDPE, such as its melting temperature and heat of fusion, were found. When simulating the melting process for the HDPE, a liquidus and solidus temperature of 402 K and 397 K were entered, respectively. Also, Larsen calculated the latent heat of fusion to be 220 kJ/kg. A density of 960 kg/m^3 was measured for the HDPE at room temperature. Since the observed viscosity for the HDPE was extremely high, it was assumed that the PCM did not face any natural convection. Therefore, natural convection was ruled out, and the heat transfer internally in the HDPE consisted only of conduction. The density for the PCM was set to a constant value of 960 kg/m^3, and dynamic viscosity was set to 200 Pas. Even though an actual value has not yet been found for the viscosity, but zero motion in the PCM was assumed, a relatively high dynamic viscosity was entered to rule out the viscous terms when gravity was enabled in the model with channels. The model with no fins did not include gravity since the problem only consisted of conduction and no natural convection. A piece-wise linear function for thermal conductivity and specific heat capacity was used for the HDPE. A tabulated overview of the property data used can be found in Appendix C.

An effective conductivity for the air void in the storage was derived during the preliminary work. This expression was made such that computations concerning this air void were simplified. The expression was made as a temperature-dependent function based on measured experimental data. A collection of the measurements can be seen in Appendix F together with the expression derived. In this way, the void could be simulated as a solid instead of a fluid, and natural convection was ruled out, diminishing the computation complexity.

Models

For the case with no channels, *Energy* and *Solidification & Melting* was enabled. The viscous model was set to *laminar*. When setting up the case with channels, all models were implemented the same way as described in Section 4.3 except for the *Solidification & Melting* model, which also was included here. The boundaries for the outside surfaces, namely the top and outer vertical surface, were set to convection, and the expression for HTC in Appendix B was entered.

The initial state for the channel flow was found before the actual transient simulation was computed since this also required a transient procedure. When the steady-state condition for a channel with an inner surface temperature of 190 °C was found, the rest of the model was patched to 190 °C, and the transient discharge process for the whole storage segment could be simulated.

4.4.2 Results

Both the transient heat transfer and the bulk temperature of the PCM were of interest when studying the results from the discharge process. Looking at Figure 4.9, one can see that the heat transfer rates for the LHTES with and without channels intersect just before 6 hours passed. This intersection appears because the storage with channels discharges itself faster than the one without channels. The storage with channels has therefore released a more considerable amount of heat up until 6 hours which can be seen from the larger area under the dashed line compared to the solid line in Figure 4.9. Also, the temperature was lower for the TES with channels compared to the one without channels at the same point which may be seen in Figure 4.10.

At just over six hours passed, the "lowest desired" heat rate of 500 W was reached for both storages at approximately the same time. The average PCM temperature was approximately 86 °C and 108 °C for the storage with and without channels, respectively, at this point. This can be seen in Figure 4.10.

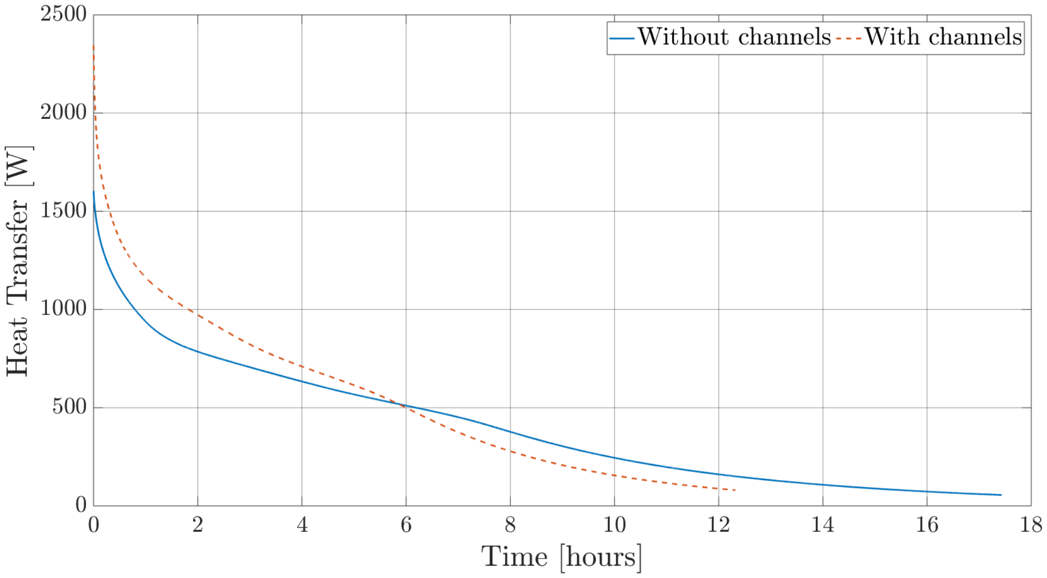

Figure 4.9: Numerical results of the total heat from the storage during discharge. The graphs pictures the discharge process for a storage with and without channels.

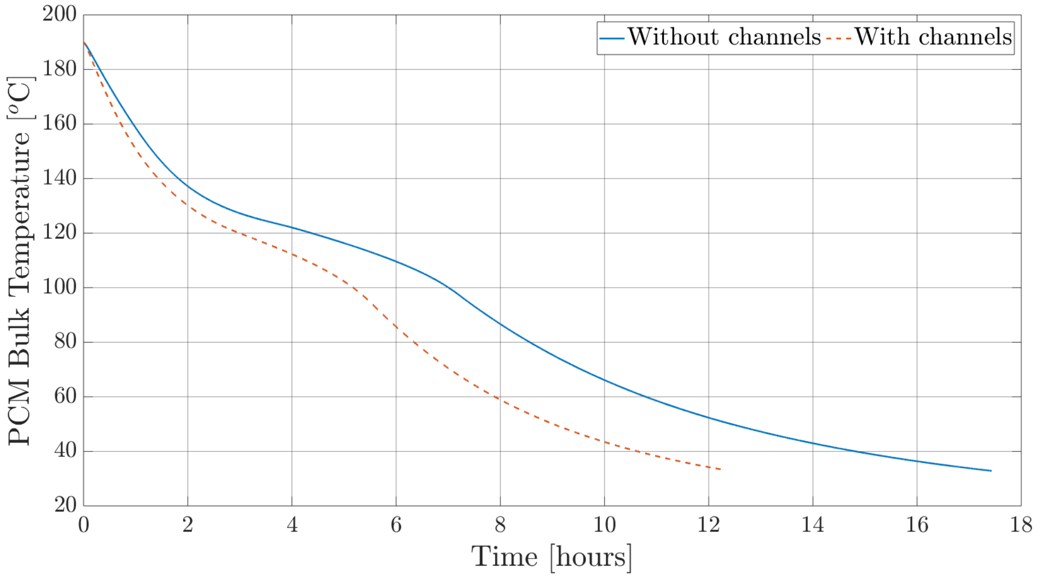

Figure 4.10: Numerical results of the change in average PCM temperature in the storage during discharge. The graphs pictures the discharge process for a storage with and without channels.

At first glance of the discharge process for the original storage without channels, it may seem like the heat rate after 8 hours was not that far from 500 W, which is true. At the same time, the average PCM temperature was almost 87 °C which is unnecessarily high. Since the stored heat was considered to exist between 60 °C and 190 °C, the storage had yet not been fully discharged after 8 hours, and there was still valuable energy left.

Watching when both storages reached a bulk temperature of 60 °C, the storage with channels reached this temperature after almost 8 hours, and a heat rate of 287 W was obtained. The storage without channels reached 60 °C after 10.8 hours and supplied a heat rate of 206 W. One of the specifications for the storage was to utilize the driving forces present down to 60 °C. As the simulation for the TES with channels presents; this temperature was reached after the desired eight hours. The only thing missing for the discharge period to satisfy the desired deliveries was the heat transfer rate to be 500 W at the discharge end. At the same time, this number may be seen as a volatile specification. Further discussion on these results will be done in the upcoming section, where the rest of the presented results during this chapter also will be discussed.

4.5 Discussion

Different aspects of the previous results from the channel calculations will be discussed in this section. One topic in this discussion will be why the heat transfer as a function of slit distance and fins behaves as it does. Comments on the different deviations between estimated and numerical computations will be made and attempted to be explained. Lastly, a more true discharge behavior will be described.

4.5.1 Analyzing the Plots from the Channel Optimizations

Two plots picturing the total heat release as a function of slit distance were presented in the section where the optimized arrangement was computated (Figure 4.4). Each heat release contribution will be analyzed isolated to observe the effects of increasing the slit distance and adding fins.

Heat Transfer from the Exterior Vertical Surface

The heat transfer from the outer surface increases when the number of fins connecting the storage and exterior wall increases. An illustration of this may be found in Appendix A, Figure A.1. As more fins are added, the margin decreases. The explanation is that the positive effect of lowering the temperature drop through the extended surface as fins are added has a decreasing margin as more fins are added.

An interesting observation from Figure A.1 is that the duty increases as the slit distance increases for each fin number. The initial thought for the heat release from the outer surface was that it would decrease as the slit distance was increased for a fixed number of fins. This hypothesis assumed that a more significant temperature drop would be obtained through the fin and exterior wall due to their increased length. The opposite was observed when looking at the isolated heat duty from the exterior surface. One explanation for this may be that as the slit distance increases, the heat transfer area of the exterior wall will also increase. The increase in heat transfer area will counteract the negative effect of the increased temperature drop through the fin. At the same time, increasing the slit distance will decrease the aspect ratio causing a smaller HTC in the channel, and a lesser heat is transferred to the channel air from the external wall. The reduced heat transfer in the channel may diminish the temperature drop through the exterior wall. The increase in the pertinent heat transfer area and decrease in HTC inside the channel seem to have a net positive effect on the outer heat transfer as the slit distance increases. The increase in the outer heat transfer as the slit distance increase is more noticeable for aluminum than cast iron. Since cast iron has a lower thermal conductivity than aluminum, the temperature drop will be more significant through the fin and exterior wall as these are extended. The negative effect in outer heat transfer from the temperature drop due to the increased "fin length" is, therefore, more dominant for cast iron than aluminum.

Heat Transfer Inside the Channel

When studying the heat exchanged in the channel, an increased number of fins does not necessarily lead to a higher heat transfer at given slit distances as it was proved for the outer heat transfer. For some slit distances, an increase in the number of fins leads to a reduced heat duty. This may be seen in Figure A.2 in Appendix A, a bit more evident for aluminum than cast iron. Slit distances ranging from approximately 12 to 20 mm for the aluminum channel indicate that a higher heat transfer is delivered when having 14 fins than 16 and 18 fins. The largest decrease in duty when having 18 fins compared to 14 is at a 15 mm slit distance. This slit distance is the same as where the increase in total heat transfer from the whole aluminum storage ceases when adding more fins than 14, as pictured in Figure 4.4. The decreased aspect ratio as the number of fins increases may explain the observed stagnation and reduction in heat transfer. A lower aspect ratio leads to a lower HTC in the channel. An increase in friction is also a result of a smaller aspect ratio. The increased friction leads to a decrease in mass flow rate, which indicates a decrease in the air flow's heat capacity rate. The time it takes for the air to flow through the channel is prolonged due to the reduced velocity. This increased time increases the air's possibility of obtaining an even higher temperature increase through the channel. Despite the hotter air temperature out of the channel, the decrease in HTC seems to be the dominating effect that causes the heat transfer rate to decrease as fins are added.

It is mainly the heat transfer from the channel flow that causes the curves to appear as they do with each peak at a given slit distance. The highest heat transfer through the channel is the point where the balance between the different positive and negative effects obtained when changing the aspect ratio gives the highest duty. A reduced heat release is obtained when moving to the left from the "optimal" slit distance. This decrease may be explained by the decrease in cross section area and the following lessening of airflow for the heat exchange. A decreased heat transfer is also obtained when moving to the right from the apex of the curves. Increasing the slit distance will increase the hydraulic diameter, which may be a positive effect since the available cross section area is increased for the heat transfer fluid. The aspect ratio will decrease as the slit distance is increased. A smaller aspect ratio leads to a smaller Nusselt number which again leads to a smaller HTC. The increased hydraulic diameter relaxes the decrease in HTC caused by the decreased Nusselt number. The aspect ratio seems to have the dominant effect on the HTC when assessing the negative effect of decreasing the aspect ratio and the positive effect of the increased hydraulic diameter.

4.5.2 Obtained "Optimal" Channel

It is already addressed that the assumption of having a fully developed flow in the channel was inadequate. Since the flow behaves differently than assumed in the optimization computations, another geometry would probably correspond to an optimal channel geometry at 60 °C. A larger heat transfer coefficient will be present when the flow is not fully developed due to the thinner boundary layer. At the same time, a larger friction factor is present, which slows down the flow, and a larger air temperature will be obtained in the channel. This increase in temperature makes the driving forces through the channel larger. The error between the estimated and numerical channel flow will be commented on later in the discussion when comparing these results more closely.

Even though the assumption of the fully developed flow proved to be incorrect, the deviation in total heat transfer was not that noteworthy when comparing the estimated and numerical results. The deviations ranged between -4.4 % and 2.6 %. The numerical results proved the enhanced heat transfer rate estimated for the design modifications to be valid. If a more accurate optimal channel geometry is desired, a closer numerical study may be done by changing the slit distance and distance between the fins. The design modifications may also need to be changed due to what may be feasible in the manufacturing process and what is desired as aesthetic manners. However, a promising enhanced heat release was proved to occur by the design modifications.

The optimal channel geometry was desired to be obtained for the conditions representing the end of the discharge process. This end was set to be when the average PCM temperature measured 60 °C. At this temperature, the driving force is starting to become insignificant. The desired capacity of 6 kWh was stored in the PCM and container for a bulk temperature between 60 °C and 190 °C. When the bulk temperature reaches 60 °C at the end of the discharging, a higher temperature is obtained in the storage center, and the PCM closest to the container wall is lower than the bulk temperature. The optimal channel geometry was obtained for a surface temperature of 60 °C. In retrospect, this boundary condition was not that suitable to be used in the optimizing computations. Since a more realistic inner channel temperature would be closer to 50 °C at the discharge end, a different channel size would probably represent the optimal heat transfer when the bulk temperature is 60 °C.

4.5.3 Deviation Between Estimated and Numerical Results

There was a deviation between the estimated and numerical heat exchanged inside the channels. The deviation between estimated and numerical heat transfer in the channel ranged between 4 % and 15 %, which is significant when reaching such high differences. The main explanation for these deviations was the assumption of having a fully developed flow when the entry length proved to be longer than the channel. Even though these deviations were significant due to the incorrect assumption, the total heat release from the whole channel did not deviate significantly. Due to deviations in the heat release from the outer surface, the total estimated and numerical heat transfer only deviated between -4.4 % and 2.6 % from each other.

The numerical computed heat released from the external surface is smaller than the estimations calculated, implying a smaller external surface temperature in the numerical model. The estimations assumed a constant mean air temperature through the channel. Since the flow proved not to be fully developed, a colder mean air temperature in the channel would be more accurate for the first part of the channel. The colder channel air would have made the external wall less hot. These deviations are more prominent for the cast iron than aluminum due to the difference in thermal conductivity. A smaller thermal conductivity leads to more significant temperature gradients in the wall and a larger deviation between the estimated and the numerically computed surface wall temperature.

As mentioned when presenting the results, the total heat transfer rate for the cast iron channel was smaller in the numerical results than estimated. For aluminum, it was the opposite. The lower heat transfer at the external surface obtained in the numerical computations had a more dominating effect on the total heat transfer when the channel was made out of cast iron than aluminum. Therefore, the large reduction in outer heat transfer outweighed the increased channel heat transfer for the cast iron channel. Due to this, the lower external surface temperature obtained in the numerical computations had a net negative effect for the cast iron channel while a net positive effect was obtained for aluminum.

A larger heat release was obtained when including radiation, which was assumed initially. Since a more significant temperature difference between the inner and outer channel wall was obtained for the cast iron than the aluminum channel, a larger potential was available when including radiation in the computations.

The Nusselt numbers used in the estimations were indicated for cases with uniform channel temperatures. Therefore, the heat transfer coefficients were somewhat incorrect since there was a temperature difference between the inner and outer channel walls. The assumption is even less correct for a cast iron channel than for an aluminum channel due to the larger temperature difference.

4.5.4 Discharge Period

When conducting the transient discharge computations, a temperature equal to room temperature was said to surround the storage walls. This may be true after a while but is a wrong assumption at the beginning of the discharge period. At the beginning of discharge, the firing process has just ended, and the air temperatures surrounding the oven and storage can therefore be assumed to be higher than the rest of the room. A higher air temperature means a lower heat transfer both from the channel and exterior surface due to smaller temperature differences and smaller driving forces. This increased surrounding air temperature causes the discharge period to last longer than computed in chapter 4. The peak at the beginning is reduced and will be flattened out, which causes a delay in the discharge process compared to the simulated results.

The charging period will be extended as the exterior wall is added to the storage. This extended duration is caused by the enhanced heat release due to the design modifications. The charging process has not been investigated in this report but is of great interest in further developing the LHTES.

A shorter discharge period would have been obtained if radiation had been included in the discharge computations. These effects would have been most significant in the beginning, as seen by comparing the results with and without radiation. The explanation is that the temperature difference between the inner and outer channel walls is larger for higher storage temperatures.

4.6 Conclusion

A study has been performed to enhance the outer heat transfer of the LHTES such that its performance would close up on the desired deliveries. A considerable thermal resistance outside the original storage wall prevented the stored heat from being released efficiently. The outer surface area was increased in an attempt to lessen the observed resistance. The introduced external surfaces consisted of walls which formed several channels on the storage's exterior vertical wall.

The enhancement study consisted of two parts. The first part consisted of simplified calculations, called estimations, to find a somewhat optimal geometry of the channels on the outer surface. The second part was more comprehensive numerical computations on the obtained channel geometry. The optimal channel geometry chosen was the arrangement that supplied the most enhanced heat release when the inner storage wall held 60 °C. By implementing the channels, the heat transfer rate from the whole storage was increased from 171 W to 310 W when the inner container wall was 60 °C. This is an 80 % enhancement.

Two different materials were used in the computations. One resembled cast iron with thermal conductivity of 50 W/(mK) and the other material with thermal conductivity of 200 W/(mK) to resemble aluminum. A more enhanced heat release was obtained using a material with larger thermal conductivity due to a more uniform temperature on the external storage walls. If the channels were made out of aluminum compared to cast iron, a 14 % increase in total heat transfer rate would be obtained when the storage wall held a temperature of 60 °C.

The reduced duration of the discharge period was a desirable outcome by enhancing the outer heat release. Since one of the project's specifications was to deliver a desired amount of 6 kWh in approximately eight hours, the design modification was indeed an improvement contributing to reaching the desired deliveries. The initial state for the discharge period was a uniform storage temperature of 190 °C. The heat stored in the container between 60 °C and 190 °C was approximately 0.8 kWh, while the PCM was charged with just above 5.2 kWh. It took just below eight hours for the modified storage to reach an average temperature of 60 °C. This temperature represented the end of the discharge period and implied that all the stored energy had been released. The total amount of heat released during a discharge period of 8 hours was increased by 13 % when implementing the channels.

As discussed earlier, the start of the discharge period would look slightly different. A lower heat release at the beginning would make the discharge period last longer. Simulating this would be of great interest.

Chapter 5

Inner Heat Transfer

Until now, this report has investigated one possibility of obtaining high heat transfer rates on the outer surfaces of the storage. Another side of the story is the inner heat transfer. The PCM, which was used during the preliminary project work and Larsen's thesis [5], had a visible high viscosity, and free convection internal in the PCM was assumed non-existent. The thermal conductivity was also found to be very low. Due to uncertainties regarding what heat fluxes will be obtained between the storage and oven, the HDPE's risk of reaching its degradation temperature at 300 °C is assumed to be considerable. From this matter, it is desired to obtain a higher heat transfer through the PCM than the conduction can provide. An interesting investigation would be to see which effects buoyancy forces may have on the heat transfer in the PCM. Studying the computed effects may give a pointer to what properties to look after when searching for a desired PCM.

To conduct this experimental study, different density gradients for the PCM were assessed for a fixed temperature gradient. Also, two different functions of viscosity in addition to different heights for a melted volume of HDPE will be used in the study. The different scenarios will be assessed as steady-state problems, and an effective conductivity will be obtained for each scenario. The buoyancy investigations were conducted using the software Ansys Fluent.

The following sections will discuss the criteria for obtaining natural convection and how a numerical model was established to investigate the possible benefits of buoyancy effects. The numerical computations will be presented and analyzed to establish the heat transfer enhancement obtained due to natural convection for the different scenarios.

5.1 Onset Natural Convection

When natural convection was presented earlier in chapter 4, the Rayleigh number was introduced. As mentioned, this parameter tells something about the buoyancy flow regime. It can also be seen as the product of the Grashof number and Prandtl number, where the Grashof number also was introduced in the same chapter. The Grashof number is, as mentioned, a relationship between buoyancy forces and viscosity forces. It is typically for a fluid's density to decrease as it experiences a temperature increase which causes buoyancy forces to act on the fluid. A force that may counter these forces are viscosity forces.

Both theoretical and experimental investigations have been done to attain a criterion for the onset of natural convection. This criterion is when the fluid flow exceeds the critical Rayleigh number, Ra_{crit}, of 1708 when considering an infinite cavity [20]. When the Rayleigh number exceeds the critical value, the buoyancy forces manage to overcome the viscosity forces, and motions will appear in the fluid [20]. The critical Rayleigh number depends on the domain's aspect ratio. For a cavity with a large aspect ratio, $w/L >> 1$, the cavity is compared with an infinite cavity where effects at the vertical walls can be neglected. The buoyancy effects will in this report be investigated for a cylinder with a diameter of 50 cm. As the aspect ratios investigated are larger than 1, the criterion for an infinite rectangular cavity is assumed to be true for the cylinders. In Figure 5.1, it is illustrated how the height of the melting volume, which is the characteristic length for the cavity, increases as the PCM melts. The increasing characteristic length will decrease the aspect ratio. This change in aspect ratio is assumed not to affect the critical Rayleigh number of 1708. Nevertheless, the change in characteristic length will affect the obtained Rayleigh number and heat transfer in the domain.

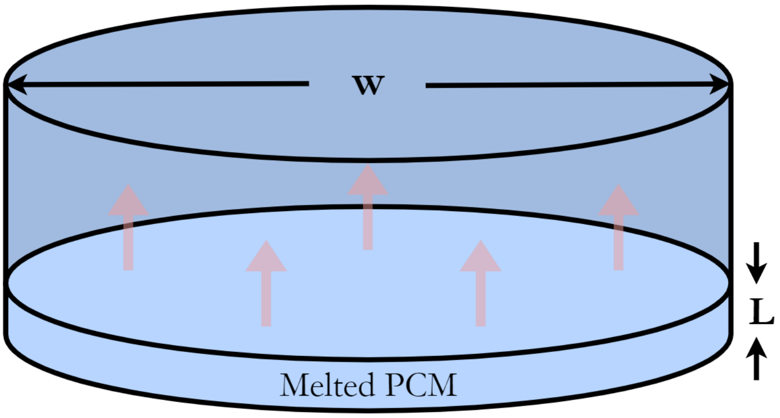

Figure 5.1: Sketch of the melted PCM volume during charging. The volume height increases as the PCM melts due to heat supplied at the bottom.

5.2 Estimating PCM Properties to Onset Natural Convection

Before the numerical examinations were conducted, a circa onset point of natural convection for different given melting heights were established. In this way, it was possible to estimate which conditions would lead to natural convection and which would not and possibly rule out some scenarios for further numerical computations.

5.2.1 Method

Some approximations were made to estimate an onset point of natural convection. The different scenarios were considered as a 2-D problems with different fixed heights. These heights represented the characteristic lengths of different melted volumes ranging from one to ten centimeters. Each scenario was examined as a steady-state problem where the temperature at the bottom and top of the volume was the same constant values for all cases, 250 °C and 124.2 °C, respectively. These temperatures were chosen since the top represented the melting front during charging and was set to the melting temperature. The bottom temperature was set to be closer to the degrading temperature of 300 °C but still having a safe distance from it. In this way, a safe increase in heat flux due to natural convection could be obtained without closing in on the degradation temperature.

Thermal properties

Some of the thermal properties of the HDPE were altered to observe what effects this could have. Since the density is only been measured to 960 kg/m^3 at solid state, this value was set to represent the density at melting temperature. The density at 250 °C was altered and tested. Also, dynamic viscosity has never been measured. Two different expressions for the dynamic viscosity were developed partly based on observations of the melted HDPE and an expression obtained from the viscous theory, which relates the dynamic viscosity and temperature. Two different expressions were made to play with different thought scenarios. The rest of the PCM's thermal properties, such as thermal conductivity and specific heat capacity, have been measured in the laboratory by Larsen. Complete data of these properties depending on temperature can be found in Appendix C.

From experiments where the HDPE was melted, its viscous behavior could seem to resemble golden syrup, which has a dynamic viscosity of 200 Pas at 13 °C [23]. Therefore, one of the experimental viscosities was said to be 200 Pas for the PCM at 400 K, which is just above its melting point. The other experimental viscosity was chosen to be 100 Pas at the same temperature to see how a lower value would affect the results. The relation between dynamic viscosity and temperature found in the literature was $\mu \propto T^{-1.6}$ [24]. This relation, together with the two chosen viscosities at 400 K, was used to carry out two different temperature-dependent expressions for dynamic viscosity, which is given in Equation (5.1). At 250 °C, the two different dynamic viscosities became approximately 65 and 130 Pas for μ_1 and μ_2, respectively. The temperatures are given in Kelvin.

$$\begin{aligned} \mu_1(T) &= 14564 51 T^{-1.6} \\ \mu_2(T) &= 2912903 T^{-1.6} \end{aligned} \tag{5.1}$$

The density gradient between the top and bottom of the fluid was altered as a variable to see when the onset point of natural convection would appear.

To conduct the desired estimations of onset points for every scenario, the expression for the Rayleigh number was altered to not explicitly be a function of temperature and the volumetric thermal expansion coefficient since this is still unknown. Instead, Ra was rewritten to be an expression of only known properties and the experimental density and viscosity changes.

Rewriting the Rayleigh Number

The approach to finding a new way to express the Rayleigh number with only known parameters was to use the approximation for volumetric thermal expansion coefficient, β. This coefficient is defined as

$$\beta = -\frac{1}{\rho}\left(\frac{\partial \rho}{\partial T}\right)_p \tag{5.2}$$

and may be simplified to

$$\beta \approx -\frac{1}{\rho_\infty}\frac{\rho_\infty - \rho}{T_\infty - T} \tag{5.3}$$

The β in the expression for Rayleigh number which was written in Equation (4.6), may be substituted by Equation (5.3). The subscript "∞" in Equation (5.3) represents the free stream, in this case, the melting front, and thus these properties will further have the subscript "m". The bottom surface represents the density and temperature in Equation (5.3) with no subscript and will be denoted with a subscript "s". The rest of the thermal properties in Ra is, as β, represented at film temperature. All thermal properties are therefore related to the surface and melting temperature in one way or another. The onset of natural convection was approximated by assessing the change in properties between the top and bottom. When substituting the thermal expansion coefficient with Equation (5.3), the new expression for the Rayleigh number could be written as

$$Ra_L = \frac{gL^3\rho^2 c_p}{\mu k}\frac{(\rho_m - \rho_s)}{\rho_m} \tag{5.4}$$

where the properties with no subscript are given at film temperature, subscript s represents the bottom surface and m the melting front. Calculating Ra for each characteristic length, dynamic viscosity, and density change between top and bottom would constitute different states where the critical value was exceeded.

5.2.2 Results

Some rough results from the estimations are given in Table 5.1 where the different density gradients needed to obtain natural convection for each characteristic length and viscosity are given. These results imply that a reasonably large density gradient between 250 °C and 124.2 °C is needed to onset natural convection for small melting heights. In contrast, a larger melting height does not require a significant density change in the material to onset natural convection.

For the numerical computations presented later, only the density gradient of 60 kg/m^3 between the top and bottom was examined. As an outcome of the conducted estimations, melting heights of one and two cm were not examined numerically since a much larger density gradient than 60 kg/m^3 was necessary for natural convection to commence.

L	**μ_1** **$\Delta\rho$**	**μ_2** **$\Delta\rho$**
10 cm	1 kg/m^3	3 kg/m^3
9 cm	2 kg/m^3	4 kg/m^3
8 cm	3 kg/m^3	5 kg/m^3
7 cm	4 kg/m^3	7 kg/m^3
6 cm	6 kg/m^3	12 kg/m^3
5 cm	10 kg/m^3	20 kg/m^3
4 cm	19 kg/m^3	39 kg/m^3
3 cm	47 kg/m^3	98 kg/m^3
2 cm	181 kg/m^3	-
1 cm	-	-

Table 5.1: Density gradient and viscosity needed to exceed the critical Rayleigh number of 1708 and for natural convection to commence for different characteristic lengths. The last three numbers are omitted since they were so large.

5.3 Numerical Computation of Enhanced Inner Heat Transfer

When investigating what effects buoyancy may have on the heat transfer through the melted PCM, the goal was to obtain an effective thermal conductivity that enhances the PCM's heat transfer when natural convection is present. A selection of the characteristic lengths presented in the section above was proceeded with for the numerical computations. Also, a fixed density gradient of 60 kg/m^3 between the melting front and bottom was used for the computations, while both expressions for dynamic viscosity from Equation (5.1) were used. Reducing the number of characteristic lengths investigated and limiting to one density gradient reduced the required number of numerically computed cases. By using the different characteristic lengths of 3, 5, 7, and 10 cm, a trend for increasing characteristic length would hopefully be obtained. A more detailed study was executed for the 5 cm tall volume where the change in heat transfer for six different density gradients was investigated instead of just one.

5.3.1 Geometry and Meshing

The geometry for the different melting volumes was a cylinder with a diameter of 50cm. This size was the same as the container for the LHTES presented in this report. Even though the LHTES-container was filled with fins, these fins were not included in these numerical models. These fins would have affected the domain's aspect ratio, where another Rayleigh number would represent the onset of natural convection. Due to the small holes in the fins, a more intricate fluid domain would be present, and the numerical computation would have become highly complex.

The CAD model was a one-twelfth section out of the whole cylindrical volume to reduce the computation duration. Four different models were made with heights of 3, 5, 7, and 10 cm. Proximity was chosen for the surface mesh, and a *maximum skewness* and *minimum* *orthogonal quality* was kept below 0.7 and above 0.1, respectively. A mesh independence study was conducted for the 5cm tall model.

Mesh Independence Study

Refining the mesh for the 5 cm tall segment, a mesh containing 147 118 cells was chosen. The mesh independence study was done by checking the maximum velocity obtained in the fluid and also the heat transfer obtained through the PCM. Graphs showing the evolution of the study can be seen in Figure 5.2.

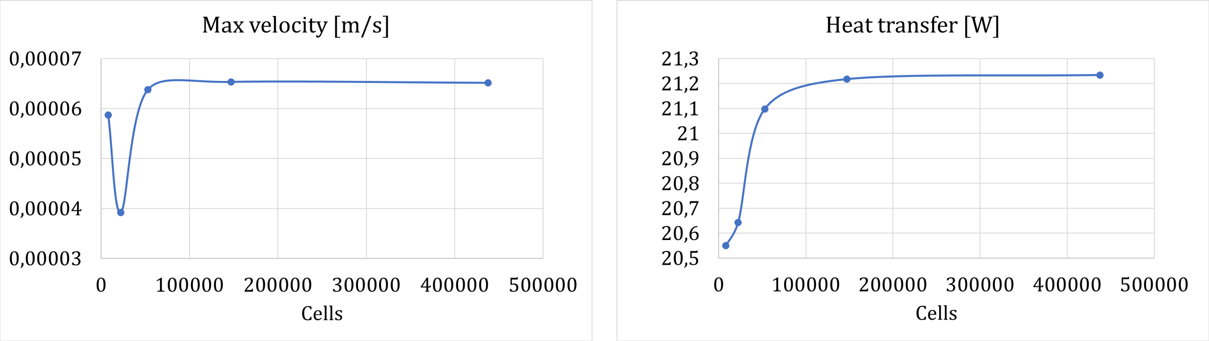

(a) Mesh independence study of maximum velocity obtained in the PCM volume.

(b) Mesh independence study of the heat transfer through the PCM volume.

Figure 5.2: Graphs from the mesh independence study conducted on the 5cm tall melting volume.

5.3.2 Models

To simulate the different steady-state problems, the transient method to calculate the buoyancy-driven flow, which was used in chapter 4 was also used for these problems due to the large temperature difference of 125.8 °C. The same procedure as in chapter 4 can be followed when choosing the different models in Ansys Fluent for these problems. From the estimations, it was found that all scenarios were in the laminar region. In addition to setting the viscous model to laminar, viscous heating was enabled. The specific operating density was set to 960 kg/m^3.

5.3.3 Boundary conditions

As for the estimations conducted earlier, steady-state was simulated numerically also. A constant bottom and top surface temperature equal to 523.15 K and 397.35 K were applied. The front surface was adiabatic, while the rest of the surfaces were set to be symmetric.

5.3.4 Results

A detailed study of what enhanced heat transfer could possible be obtained with different fluid properties at a fixed melting height of 5 cm was conducted. These results will be presented first, followed by a study made for different fixed melting heights with two different dynamic viscosities and one fixed density gradient between the hot bottom and melting front in the top. An effective thermal conductivity is obtained for each scenario to observe the improved heat transfer. This is found by using Fourier's law: $q'' = k_{eff}\Delta T/L_C$.

Studying the Effects by Changing Density

A detailed investigation was conducted for the 5cm tall volume. For this melting height, 12 different simulations were conducted. These were six simulations per each dynamic viscosity expression (μ_1 and μ_2) where the density gradient between the bottom and top was altered from zero to 60 kg/m^3 with a step length of 10. The melting front density was held constant at 960 kg/m^3.

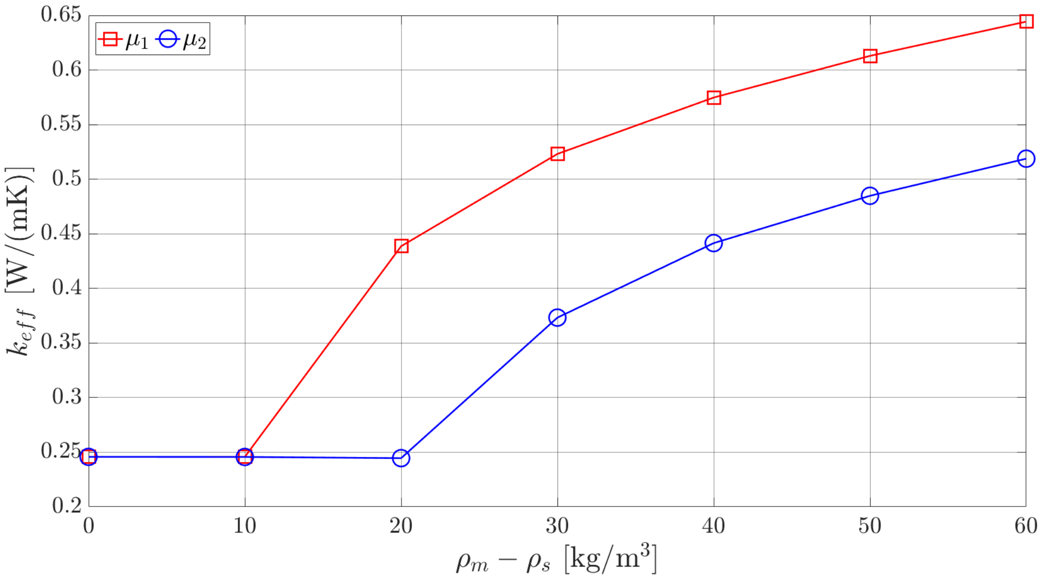

Figure 5.3: These graphs present the effective conductivity obtained in a melted PCM of 5 cm height for a variety of density gradients between bottom and top for two different viscosities.

The evolution in effective thermal conductivity for the 5 cm tall melting volume may be studied in Figure 5.3 as a function of density gradient and dynamic viscosity. An increasing effect is obtained with decreasing margin as the density gradient increases. If a density gradient of 60 kg/m^3 is obtained, an effective conductivity of 0.644 and 0.519 W/(mK) would be obtained for μ_1 and μ_2, respectively. Comparing these effective thermal conductivities to the material's actual thermal conductivity for the HDPE at the pertinent temperatures, an increase of approximately 162 % and 111 % is obtained for each viscosity, respectively. These effective thermal conductivities are proportional to the heat fluxes transferred through the melted volume for each case. A 162 % larger heat flux could therefore be supplied at the storage bottom and remaining a surface temperature of 250 °C. An equally large heat flux supplied at the bottom and no natural convection apparent could most likely lead to the PCM overheating.

When no natural convection is apparent in the 5 cm tall melted volume, a heat flux of 615 W/m^2 may be transferred through the PCM when the bottom is holding a temperature of 250 °C. The heat fluxes possible when having a density change of 60 kg/m^3 for μ_1 and μ_2 can be estimated to 1 614 W/m^2 and 1 299 W/m^2, respectively. Due to natural convection, a heat flux may be more than doubled without risking overheating the PCM. The nominal duty of a wood stove used in this project is 5 kW. Since the heat flux between the wood stove and the storage has not been examined yet, it is difficult to say how large part of the nominal duty will be supplied the storage. However, if the storage is desired to be charged in three hours, a heat transfer rate should at least be in the order of 2 kW. This corresponds to a heat flux of 10 204 W/m^2. This magnitude is significantly larger than the ones obtained in the scenarios where 5 cm of the PCM has melted.

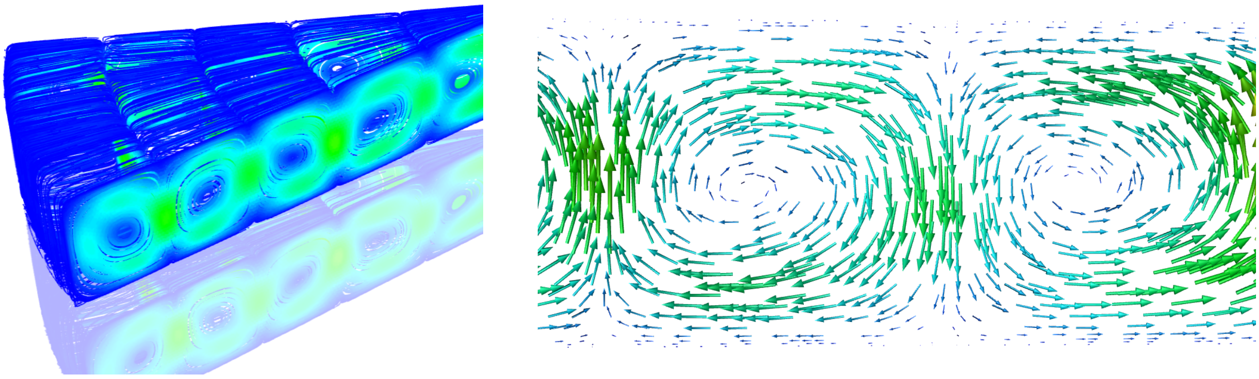

(a) Resulting pathlines in a 5 cm tall melting volume of HDPE where natural convection is obtained.

(b) Illustration of the counter acting directions of the cells developed in the melted HDPE.

Figure 5.4: Pathlines obtained from the fluid motion of the melted HDPE.

The fluid motion in the 5 cm tall volume is pictured in Figure 5.4a as pathlines. For Rayleigh numbers between 1708 and 50 000, the motion of the fluid will form regularly spaced counter-rotating cells[20]. This is seen in Figure 5.4a where the rotating cells occur as longitudinal rolls. Since the numerical domain is one segment out of a full circle, these cells will take place all the way around in the cylindrical melting volume, where each longitudinal cell lays at a constant radius. The counteracting direction of the cells may be observed in Figure 5.4b. The flow pattern will look different for the 10 cm tall melting volume when assuming μ_1 as dynamic viscosity since the domain's Rayleigh number exceeds 50 000 for this condition.

Studying Change in Melting Heights

In Figure 5.5, the results for the cases with different melting heights are viewed. These cases consist of different melting heights and a constant density gradient of 60 kg/m^3 between the top and bottom of the melting volume. When studying the results, a larger effective thermal conductivity was obtained for increasing melting height. The effective thermal conductivity for each computed scenario is reproduced in Table 5.2. A relative thermal conductivity, k_r, is also presented in the table, which was obtained by $k_r = k_{eff}/k_{actual}$.

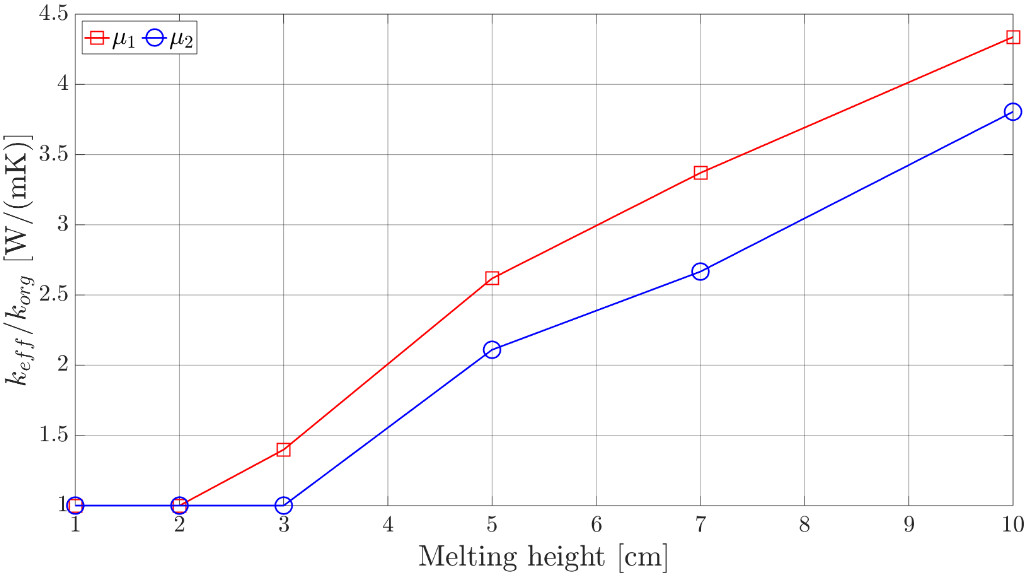

Figure 5.5: A graphical representation of the simulated results. The relative thermal conductivity obtained for different melting height when the density gradient between top and bottom is 60 kg/m^3.

	μ_1		μ_2	
L$_c$ [cm]	**k$_{eff}$**	**k$_{eff}$/k$_{actual}$**	**k$_{eff}$**	**k$_{eff}$/k$_{actual}$**
3	0.344 W/(mK)	1.40	0.246 W/(mK)	1.00
5	0.644 W/(mK)	2.62	0.519 W/(mK)	2.11
7	0.829 W/(mK)	3.37	0.656 W/(mK)	2.67
10	1.067 W/(mK)	4.34	0.936 W/(mK)	3.80

Table 5.2: Numerical results obtained for the different scenarios. An effective thermal conductivity is calculated and also the relative thermal conductivity is presented for each melting height and dynamic viscosity.

Since the effective thermal conductivity is proportional to the heat flux transferred through the material, the relative thermal conductivity would be proportional to the ratio between the heat flux transferred through the material with natural convection compared to without natural convection. A melting height of 10 cm would be able to transfer a 4.34 times large heat flux when natural convection may be present compared to having no fluid motion. This equals a heat flux of 1337 W/m^2 supplied instead of 104 W/m^2. A larger heat flux may cause the material to melt faster, and the charging time would decrease.

The effective thermal conductivity increases as the melting height increases. A natural explanation for this is that as the characteristic length increases, the Rayleigh number will also increase since $Ra \propto L_c^3$. A higher Ra indicates larger buoyancy forces compared to viscous forces, which indicate more motion and, therefore, more natural convection. Figure 5.5 displays an increasing function with decreasing margin. From the theory, a proportional relation between the relative thermal conductivity and the characteristic length is found to be $k_r \propto L_c^{3/4}$. This relation is true in the laminar region when heat is added at the bottom. The derivation of the proportionality may be found in Appendix G. Two proportional constants were tried to be obtained, one for each viscosity. A constant $C_1 = 24.64$ and $C_2 = 20.32$ was found for the dynamic viscosity μ_1 and μ_2, respectively. The constants computed for the 3 cm melting volume deviated significantly from the constants. A plot of the proportionality constants may be found in Appendix G.

In Figure 5.6, the flow patterns for a 7 and 10 cm tall melted volume are pictured. The pattern assumed to look different for the 10 cm tall volume than for the 5 cm tall volume pictured in Figure 5.4. This was because the Rayleigh number for the 10 cm volume was estimated to exceed 50 000. The 7 cm tall volume was assumed to consist of longitudinal rotating cells as in the 5 cm tall volume because of its estimated Rayleigh number.

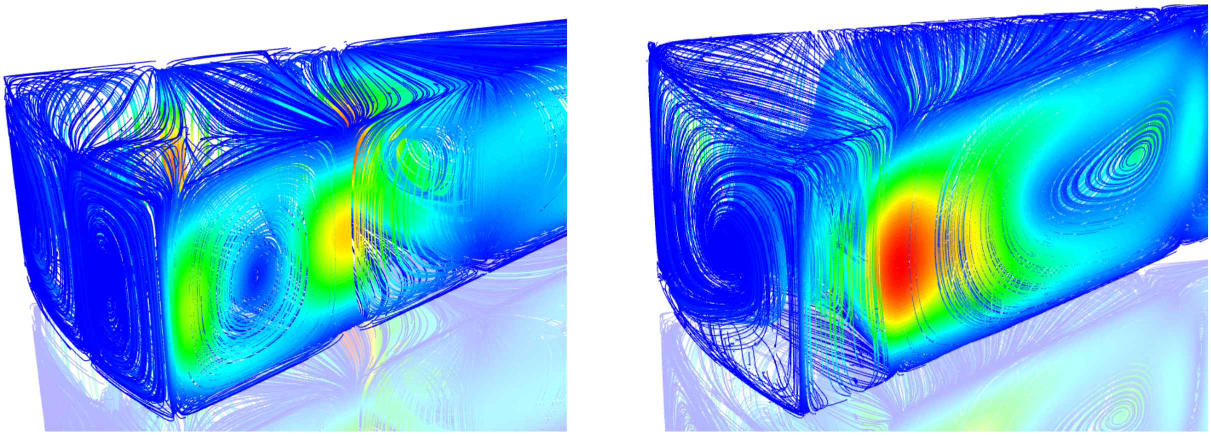

(a) Pathlines of the fluid motion in the 7 cm tall domain. The density gradient was 60 kg/m^3 and the dynamic viscosity was set to μ_1.

(b) Pathlines of the fluid motion in the 10 cm tall domain. The density gradient was 60 kg/m^3 and the dynamic viscosity was set to μ_1.

Figure 5.6: Pictures of the different fluid pattern for two different melting heights.

5.4 Discussion

This section will discuss the results presented during this chapter. The quality of the different assumptions will be brought up. Deviations between assumed and obtained flow patterns will also be commented on.

5.4.1 Conditions Representing Onset of Natural Convection

The estimations conducted in the first part of this study were based on simplifications. Since the thermal expansion coefficient was unknown, a simplification was used to alter the expression for the Rayleigh number. The estimated results were reproduced by rounding up to the nearest integer for simplicity. This approximated study was conducted as preparation for the numerical study. It was used as a pointer for which cases would be interesting to investigate numerically, and may not be assumed to be exact numbers representing the reality.

The estimated results implied that the onset point of natural convection for the 5cm tall melting volume would be a density gradient of 10 and 20 kg/m^3 for μ_1 and μ_2, respectively. From the numerical computations for the 5 cm tall melting volume, it may look like the same density gradients corresponded to the onset of natural convection, but this may not be exact. Since the step size for each simulation of the 5 cm tall volume was as large as 10 kg/m^3, the actual onset point for each viscosity may be either before or after 10 and 20 kg/m^3. Despite this, the estimations seem not to be too far away from the truth for when natural convection will occur. The presented procedure of estimating what conditions may cause natural convection seems to be a good way to do easy calculations on new materials.

5.4.2 Effects from Increasing Density Gradient

The 5cm tall melting volume's results show that the effective thermal conductivity increases as the density gradient between the top and bottom increases. The curves indicate that this increased effect will decrease as the density changes keep on growing. This trend is due to the relative thermal conductivity being proportional to the Rayleigh number to the power of one-fourth, which again is an expression containing the fluid densities. The final proportionality between the relative thermal conductivity and the densities becomes $k_r \propto (\rho_{avg}^2(\rho_m - \rho_s)/\rho_m)^{1/4}$. From this, it is clear that the margin decreases as the density change in the domain increases, which was shown in the results for the 5cm tall melted volume.

5.4.3 Increase in Tolerable Heat Flux

The reason why natural convection is desired is to reduce the risk of overheating the PCM. This increase in manageable heat flux tells that a larger heat flux may be supplied from the wood stove top without closing in on the degradation temperature.

Even though the free convection enhances the heat transfer, the mixing of the material may lead to an increased speed of oxidizing the material. Also, a reduced material weight may occur due to evaporating material which is also speeded up when mixing the material.

5.4.4 Relevant CAD-model

The numerical study presented above may not be used directly for the actual storage container. If the numerical computations had included the present fins, a very complex problem would have been obtained due to the small holes in the fins. This viscous study was simplified from the existing container to not containing the fins to make a more general study on what effects may be obtained by fluid motions for different thermal properties.

If the fins were to be considered, the domain's aspect ratio would be much smaller than assumed. These new cavities could no longer be accounted for as infinite because the viscous effects at the fin walls could no longer be neglected. If natural convection is supposed to appear in between the fins in the existing container, an even less viscous fluid is needed since the internal fins will slow down the fluid motion due to the no-slip condition at the walls. The critical Rayleigh number will increase as the aspect ratio decreases since more viscous forces will be present, and even more buoyancy forces are needed to oppose these forces.

It may seem like the CAD model being only one-twelfth part of the total melted cylindrical volume, may have been too small to obtain the correct fluid motions. From the theory, longitudinal rotating cells were said to exist for Rayleigh numbers between 1708 and 50 000. The estimated Rayleigh numbers obtained for density gradient of 60 kg/m^3 were safely within these limits except for the two 10cm tall melted volumes. The estimated Rayleigh number for the 10 cm melting volume and a dynamic viscosity equal to μ_1 exceeded 50 000. The streamlines in the volumes with Rayleigh numbers close to or above 50 000 could have been assumed not to have longitudinal rotating cells. On the other hand, both the scenarios for 7 cm melted volumes were assumed to consist of longitudinal rotating cells. This was not the case when looking at the pathlines for the 7 cm tall melting volumes. Instead, there was a more complicated streamlined pattern obtained. A too small segment being the CAD model may have caused this. Another explanation may be that the aspect ratio did not satisfy the conditions to be acknowledged as an infinite cavity ($w/L >> 1$). It is difficult to say if the complex streamlines form Rayleigh-Benard cells or another pattern.

5.4.5 Reliability of the Numerical Results

There are some insecurities in the numbers obtained from the numerical computations. The transient method was utilized to find a steady state of the natural convection for the different cases. This proved to be a time-demanding study where the computations struggled with converging to a steady solution. Small oscillations were observed. These oscillations represented minor variations, and circa values were chosen for the final results presented. Even though the extracted heat fluxes and effective thermal conductivities may deviate from an exact episode, the trends remain. It became more difficult for the larger domains to converge than the smaller fluid domains. Due to the higher Rayleigh number, as the characteristic length increased, a transition state would possibly be close, making it difficult for the solution to find a steady state.

The constants obtained for the proportional relation seemed to agree reasonably well for the three tallest melting volumes, while the constant obtained for the 3 cm tall melting volume differed. One reason for this may be that the calculation had not yet converged completely.

5.4.6 Choice of Viscosity

From the results presented, both in the estimated and the numerical results, it may look like natural convection occur for large melting volumes. Based on the estimated results, only a minimal density change seemed required to onset natural convection. Since non-existing motions in the melted HDPE had already been observed during previously conducted experiments, the assumed dynamic viscosities of 100 and 200 Pas at 400 K were most likely incorrect.

5.4.7 Realistic Charging Behavior

The evolution of effective thermal conductivity as the characteristic length increases cannot be compared to the evolution as the melting height increases during an actual charging process. The reason is that the bottom temperature of the storage will most likely not stay constant as heat is transferred to the storage during charging. This is assumed since the thermal conductivity decreases as the material melts. A decreasing thermal conductivity would cause the material to be heated. For a constant temperature to be obtained at the storage bottom, a non-constant heat flux would be required since the thermal resistance through the PCM volume changes as it is heated. A more realistic assumption would be to obtain a heat flux following the shape of a principle sketch of the heat transfer obtained from a wood stove during a firing process. The unknown resistance between the stovetop and storage bottom may affect the heat flux obtained. These effects have not yet been investigated. Therefore, it may be challenging to say anything about how large heat fluxes that will occur. The heat fluxes are again what decides what temperatures may occur at the storage bottom.

5.5 Conclusion

This chapter aimed to examine the effects of natural convection on a heated fluid and see how much higher heat fluxes could be tolerable for fixed boundary conditions than if no natural convection was present. During this chapter, some basic buoyancy theory was explained, and the criteria to onset natural convection in an infinite cavity was introduced. Some estimations were conducted to approximate what material properties would onset natural convection for different melted volumes. An experimental, numerical study was executed to observe the effects of natural convection in an experimental PCM.

A critical Rayleigh number of 1708 represents the onset of natural convection for a fluid domain with a large aspect ratio. The critical number will increase for smaller aspect ratios since the viscous effects at the vertical walls will become more prominent. Even larger buoyancy forces will be required to overcome the viscous forces in the fluid. From the results, it is clear that the characteristic length of the melted domain may have a lot to say about if motions will appear or not. Small characteristic lengths will limit the Rayleigh number from reaching its critical value and also limit motion to appear in the fluid domain. If the distance between the vertical surfaces is small enough, the viscid effects from these surfaces will slow down the fluid motion, causing the natural convection to decline or cease.

The method used to estimate if the critical Rayleigh number exceeded for different fluid conditions seemed to perform reasonable estimates. This method may be used later when evaluating if a material may undergo natural convection or not.

When natural convection occurs in a fluid domain, higher heat fluxes may be transferred through the domain compared to the heat fluxes transferred by only conduction. The increase in heat flux depends on the domain's Rayleigh number, which is a function of the fluid's dynamic viscosity, temperature-dependent density, and the domain's characteristic length. During this experimental, numerical study, constant boundary conditions were applied. The bottom was set to 250 °C, and the top represented the melting front in the PCM, having a constant temperature of 124.2 °C. The enhanced heat flux by attaining natural convection would reduce the risk of overheating the PCM during a firing process. When the tallest investigated melting volume experienced natural convection, a 4.34 and 3.80 times higher heat flux could be supplied and still obtain the same boundary conditions. These two numbers were obtained using the dynamic viscosities μ_1 and μ_2, respectively.

The HDPE used in the existing storage risks overheating at large heat fluxes due to its small thermal conductivity and high viscosity. By introducing natural convection, a higher heat flux will be manageable for the PCM to retain a safe temperature and reduce the risk of overheating.

Since the viscosity of the utilized HDPE is not measured, it is not easy to draw any conclusions as to what criteria would onset natural convection for the material. Also, the assumption of an infinite cavity is not comparable to the existing storage design. What heat fluxes may be obtained at the storage bottom is still unknown. Therefore, a specific conclusion of what properties may be essential for the storage material is not that easy to say.

Chapter 6

Conclusion

The report's objectives was to study how the outer and inner heat transfer could be enhanced for an LHTES on a wood stove. First, a brief presentation of different PCM applications was made before more technical subjects was dived into. The technical investigations involved both approximated estimates and further more comprehending numerical computations was conducted to obtain more detailed and accurate results. The upcoming two sections are a copy of the conclusions made in Chapter 4 and 5.

6.1 Enhanced Outer Heat Transfer

A study has been performed to enhance the outer heat transfer of the LHTES such that its performance would close up on the desired deliveries. A considerable thermal resistance outside the original storage wall prevented the stored heat from being released efficiently. The outer surface area was increased in an attempt to lessen the observed resistance. The introduced external surfaces consisted of walls which formed several channels on the storage's exterior vertical wall.

The enhancement study consisted of two parts. The first part consisted of simplified calculations, called estimations, to find a somewhat optimal geometry of the channels on the outer surface. The second part was more comprehensive numerical computations on the obtained channel geometry. The optimal channel geometry chosen was the arrangement that supplied the most enhanced heat release when the inner storage wall held 60 °C. By implementing the channels, the heat transfer rate from the whole storage was increased from 171 W to 310 W when the inner container wall was 60 °C. This is an 80 % enhancement.

Two different materials were used in the computations. One resembled cast iron with thermal conductivity of 50 W/(mK) and the other material with thermal conductivity of 200 W/(mK) to resemble aluminum. A more enhanced heat release was obtained using a material with larger thermal conductivity due to a more uniform temperature on the external storage walls. If the channels were made out of aluminum compared to cast iron, a 14 % increase in total heat transfer rate would be obtained when the storage wall held a temperature of 60 °C.

The reduced duration of the discharge period was a desirable outcome by enhancing the outer heat release. Since one of the project's specifications was to deliver a desired amount of 6 kWh in approximately eight hours, the design modification was indeed an improvement contributing to reaching the desired deliveries. The initial state for the discharge period was a uniform storage temperature of 190 °C. The heat stored in the container between 60 °C and 190 °C was approximately 0.8 kWh, while the PCM was charged with just above 5.2 kWh. It took just below eight hours for the modified storage to reach an average temperature of 60 °C. This temperature represented the end of the discharge period and implied that all the stored energy had been released. The total amount of heat released during a discharge period of 8 hours was increased by 13 % when implementing the channels.

As discussed earlier, the start of the discharge period would look slightly different. A lower heat release at the beginning would make the discharge period last longer. Simulating this would be of great interest.

6.2 Enhanced Inner Heat Transfer

This chapter aimed to examine the effects of natural convection on a heated fluid and see how much higher heat fluxes could be tolerable for fixed boundary conditions than if no natural convection was present. During this chapter, some basic buoyancy theory was explained, and the criteria to onset natural convection in an infinite cavity was introduced. Some estimations were conducted to approximate what material properties would onset natural convection for different melted volumes. An experimental, numerical study was executed to observe the effects of natural convection in an experimental PCM.

A critical Rayleigh number of 1708 represents the onset of natural convection for a fluid domain with a large aspect ratio. The critical number will increase for smaller aspect ratios since the viscous effects at the vertical walls will become more prominent. Even larger buoyancy forces will be required to overcome the viscous forces in the fluid. From the results, it is clear that the characteristic length of the melted domain may have a lot to say about if motions will appear or not. Small characteristic lengths will limit the Rayleigh number from reaching its critical value and also limit motion to appear in the fluid domain. If the distance between the vertical surfaces is small enough, the viscid effects from these surfaces will slow down the fluid motion, causing the natural convection to decline or cease.

The method used to estimate if the critical Rayleigh number exceeded for different fluid conditions seemed to perform reasonable estimates. This method may be used later when evaluating if a material may undergo natural convection or not.

When natural convection occurs in a fluid domain, higher heat fluxes may be transferred through the domain compared to the heat fluxes transferred by only conduction. The increase in heat flux depends on the domain's Rayleigh number, which is a function of the fluid's dynamic viscosity, temperature-dependent density, and the domain's characteristic length. During this experimental, numerical study, constant boundary conditions were applied. The bottom was set to 250 °C, and the top represented the melting front in the PCM, having a constant temperature of 124.2 °C. The enhanced heat flux by attaining natural convection would reduce the risk of overheating the PCM during a firing process. When the tallest investigated melting volume experienced natural convection, a 4.34 and 3.80 times higher heat flux could be supplied and still obtain the same boundary conditions. These two numbers were obtained using the dynamic viscosities μ_1 and μ_2, respectively.

The HDPE used in the existing storage risks overheating at large heat fluxes due to its small thermal conductivity and high viscosity. By introducing natural convection, a higher heat flux will be manageable for the PCM to retain a safe temperature and reduce the risk of overheating.

Since the viscosity of the utilized HDPE is not measured, it is not easy to draw any conclusions as to what criteria would onset natural convection for the material. Also, the assumption of an infinite cavity is not comparable to the existing storage design. What heat fluxes may be obtained at the storage bottom is still unknown. Therefore, a specific conclusion of what properties may be essential for the storage material is not that easy to say.

Chapter 7

Further work

Suggestions for further work will be the last thing presented in this thesis. Different thoughts and ideas which have come to light during the proceeded work may be necessary to establish the benefits and effects from. Some of these suggestions will consider validating the conducted work, while other suggestions may be to investigate new ideas that may improve the storage performance.

Experimental validation
Since the storage's performance of the design modifications is only evaluated numerically, a validation of these results would be of interest. Such validation may be essential to rule out possible errors made when the numerical models were carried out. Therefore, a laboratory setup including the external channels would be of interest to measure and validate the computations and performance.

Further numerical investigations
Numerical investigations conducted using a more realistic surrounding temperature at the beginning of the discharge period will be of interest to obtain a more realistic heat transfer curve during discharging.

Since the charging process will be highly affected by the modified design, numerical computation of the charging process is also of great interest.

Investigate further measures for outer enhancement
A more detailed inspection of the positive and negative effects obtained by implementing tubes through the storage to enhance the outer heat transfer may be interesting. The study should investigate the adverse effects by removing possible storage capacity against the positive effect obtained by utilizing the energy stored in the hot storage center.

Obtain an Actual Firing Process
Investigate how the oven and storage behavior will be during an actual firing process. Observe how the heat flux behaves and what temperatures may be obtained between the stove and storage bottom. This study is of interest since the knowledge is short concerning how crucial it is to do measures to prevent the PCM from overheating.

Further Searching for Suitable PCMs
The conducted work made it clear that free convection in a PCM would increase the heat

transfer and reduce the risk of overheating. A search for PCM which may experience natural convection is of interest.

Bibliography

[1] Oslo Economics / Asplan Viak. *Kartlegging og vurdering av potensial for effektivisering av oppvarming og kjøling i Norge*. Ekstern rapport. 2020.

[2] Hans Magnus Kure. *Strømforbruk i norske husholdninger*. Fordypningsprosjekt. 2011.

[3] Nicolai Feilber and Bjørn Grinden. *Ny kunnskap om fordeling av strømforbruket*. Poster.

[4] SSB. *Use of wood in residential buildings*. URL: https://www.ssb.no/statbank/table/11563/tableViewLayout1/ (visited on 7th Mar. 2022).

[5] Chris-André Bastin Larsen. 'Latent heat thermal energy storage from wood stoves with high-density polyethylene as phase change material'. MA thesis. NTNU, 2021.

[6] Sara Sofie Øverbø Lindegård. 'Using a cellular metal structure to improve the thermal performance of a latent heat storage system'. MA thesis. NTNU, 2020.

[7] Henning Hvål Mathisen. 'Experimental design and testing of a PCM-based heat storage unit for wood stoves'. MA thesis. NTNU, 2019.

[8] MNA Hawlader, MS Uddin and Mya Mya Khin. 'Microencapsulated PCM thermal-energy storage system'. In: *Applied energy* 74.1-2 (2003), pp. 195–202.

[9] Luisa F Cabeza et al. 'Materials used as PCM in thermal energy storage in buildings: A review'. In: *Renewable and Sustainable Energy Reviews* 15.3 (2011), pp. 1675–1695.

[10] R Arivazhagan et al. 'Performance analysis of concrete block integrated with PCM for thermal management'. In: *Materials Today: Proceedings* 22 (2020), pp. 370–374.

[11] Marco Deckert et al. 'Economic efficiency of mobile latent heat storages'. In: *Energy Procedia* 46 (2014), pp. 171–177.

[12] Ahmad El Mays et al. 'Using phase change material in under floor heating'. In: *Energy Procedia* 119 (2017), pp. 806–811.

[13] Ekrem Tunçbilek et al. 'Thermal performance based optimization of an office wall containing PCM under intermittent cooling operation'. In: *Applied Thermal Engineering* 179 (2020), p. 115750.

[14] Eduard Oró, Alvaro De Gracia and Luisa F Cabeza. 'Active phase change material package for thermal protection of ice cream containers'. In: *International journal of refrigeration* 36.1 (2013), pp. 102–109.

[15] Sakamon Devahastin and Saovakhon Pitaksuriyarat. 'Use of latent heat storage to conserve energy during drying and its effect on drying kinetics of a food product'. In: *Applied thermal engineering* 26.14-15 (2006), pp. 1705–1713.

[16] Mohammad Saleh Barghi Jahromi et al. 'Recent progress on solar cabinet dryers for agricultural products equipped with energy storage using phase change materials'. In: *Journal of Energy Storage* 51 (2022), p. 104434.

[17] Weisan Hua, Liyu Zhang and Xuelai Zhang. 'Research on passive cooling of electronic chips based on PCM: A review'. In: *Journal of Molecular Liquids* 340 (2021), p. 117183.

[18] Hamidreza Behi, Morteza Ghanbarpour and Mohammadreza Behi. 'Investigation of PCM-assisted heat pipe for electronic cooling'. In: *Applied Thermal Engineering* 127 (2017), pp. 1132–1142.

[19] Yusuke Tomizawa et al. 'Experimental and numerical study on phase change material (PCM) for thermal management of mobile devices'. In: *Applied Thermal Engineering* 98 (2016), pp. 320–329.

[20] Frank P. Incropera et al. 'Fundamentals of heat and mass transfer 7th edition'. In: John Wiley Sons. Chap. 9.

[21] Ansys Inc. *The Boussinesq model*. URL: https://www.afs.enea.it/project/neptunius/docs/fluent/html/ug/node470.htm#uns-sec-boussinesq (visited on 21st Apr. 2022).

[22] Ansys Inc. *Natural Convection and Buoyancy-Driven Flows*. URL: https://www.afs.enea.it/project/neptunius/docs/fluent/html/ug/node470.htm (visited on 21st Apr. 2022).

[23] Volcanology analogues. *Properties for Syrup*. URL: https://sites.google.com/site/volcanologyanalogues/home/syrup (visited on 26th May 2022).

[24] M. E. Crawford W. M. Kays. 'Convective heat and mass transfer Second Edition'. In: McGraw-Hill Book Company. Chap. 14.

Appendix

A Additional Results from Channel Estimations

A.1 Heat Transfer Obtained from the Outer Extended Surface

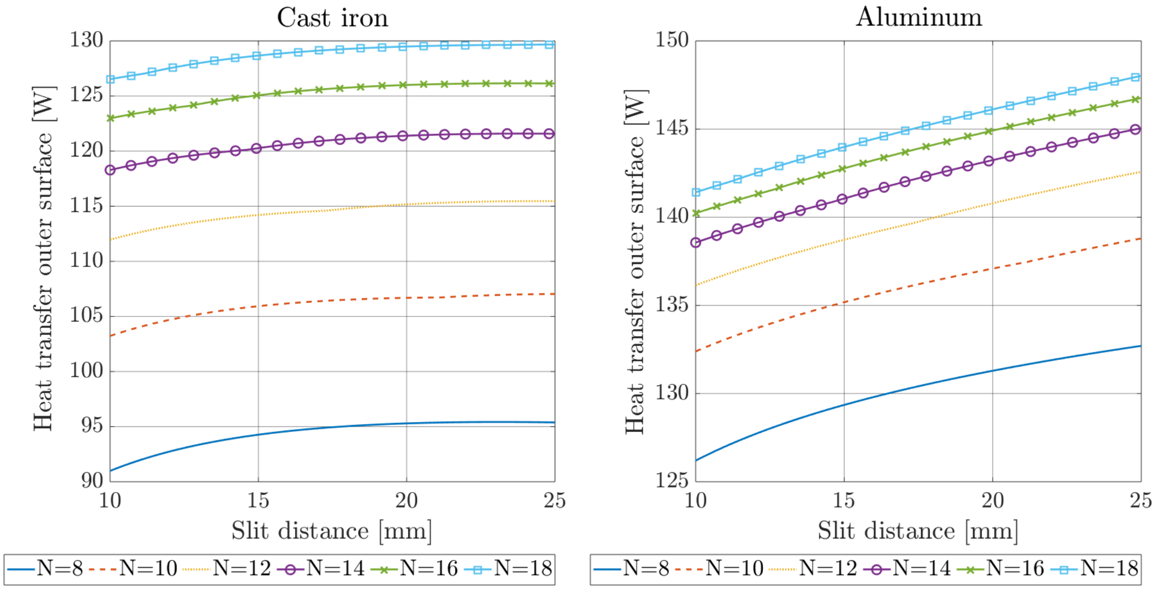

Figure A.1: Heat release from outer surface as a function of slit distance. The different curves represent different number of fins attaching the extended surface to the storage.

A.2 Heat Transfer Obtained Through the Channel

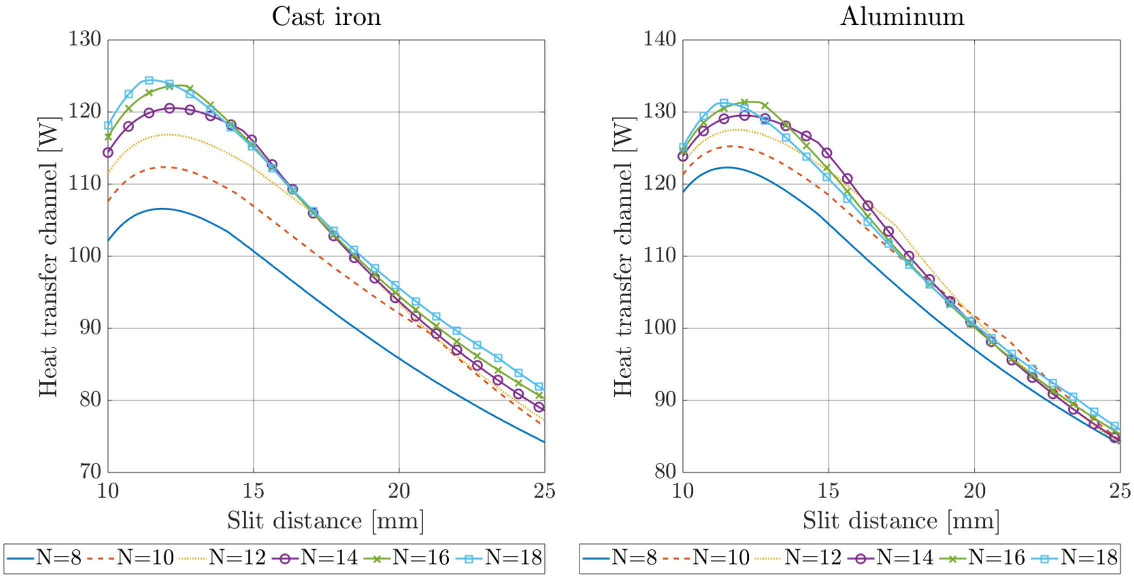

Figure A.2: Heat exchange through the channel as a function of slit distance. The different curves represent different number of fins attaching the extended surface to the storage.

B Heat Transfer Coefficient (HTC)

The obtained expressions for a collective HTC from natural convection and radiation at both a vertical and horizontal surface were two fourth ordered expressions as a function of surface temperature. The expressions are plotted together with the actual functions to picture the resemblance. Figure B.1 and Figure B.2 pictures the HTC at a vertical and horizontal wall respectively. The respective expressions are written below each figure.

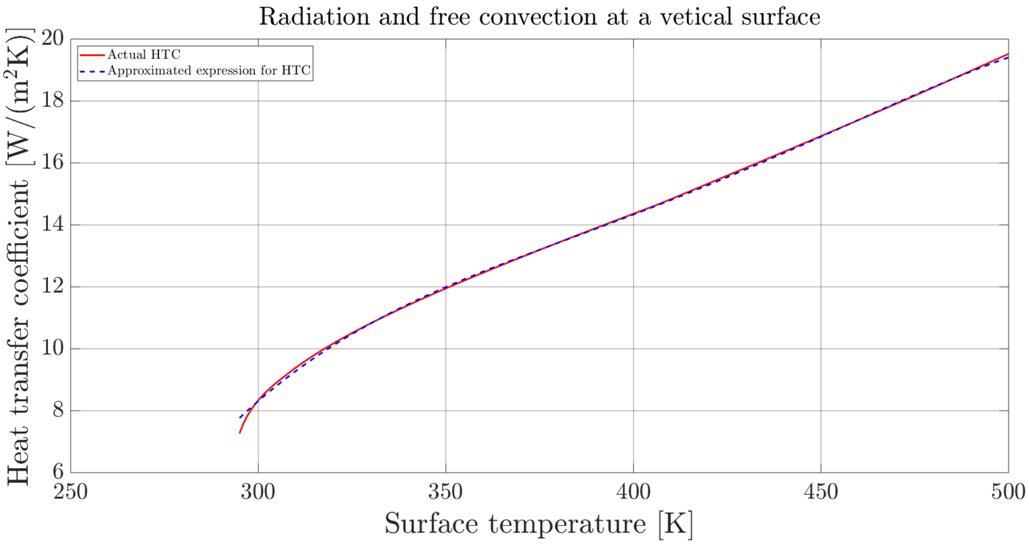

Figure B.1: HTC at a vertical wall as a function of surface temperature.

$$h_{vertical} = -1.0919E{-}08T_s^4 + 1.83895E{-}05T_s^3 - 0.0115236607T_s^2 + 3.2335207283T_s - 332.6882014268$$

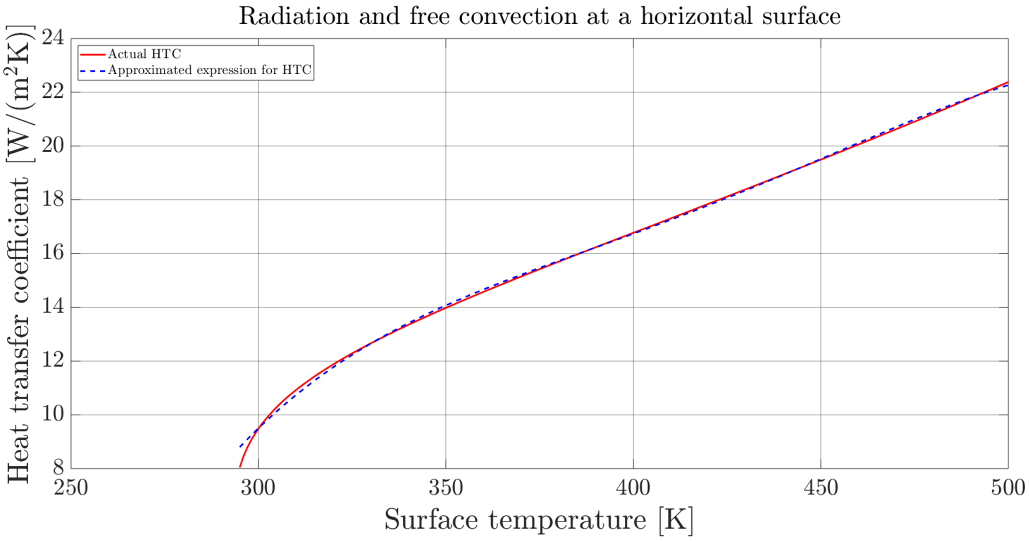

Figure B.2: HTC at a horizontal wall as a function of surface temperature.

$$h_{horizontal} = -1.4350E{-}08T_s^4 + 2.42088E{-}05T_s^3 - 0.0152166510T_s^2 + 4.2780531603T_s - 441.8201217579$$

C Thermal properties for HDPE

C.1 Specific heat capacity

Temperature [K]	**c_p [kJ/(kgK)]**
290	1.89
320	2.57
330	2.64
340	2.71
350	2.78
360	2.85
370	2.91
380	2.97
390	3.02
400	3.08
410	3.13
420	3.18
430	3.20
480	3.30

Table C.1: Specific heat capacity for the high-density polyethylene dependent of temperature.

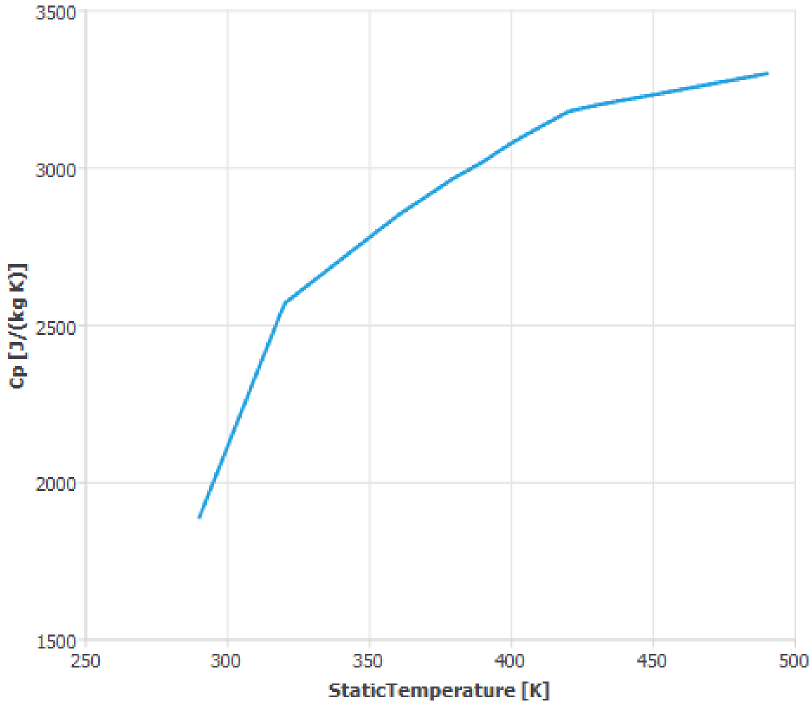

Figure C.1: Graph picturing the piece-wise linear function for specific heat capacity.

C.2 Thermal conductivity

Temperature [K]	**Thermal conductivity [W/(mK)]**
290	0.54
370	0.4
400	0.3
490	0.21

Table C.2: Thermal conductivity for the high-density polyethylene dependent of temperature for the HDPE.

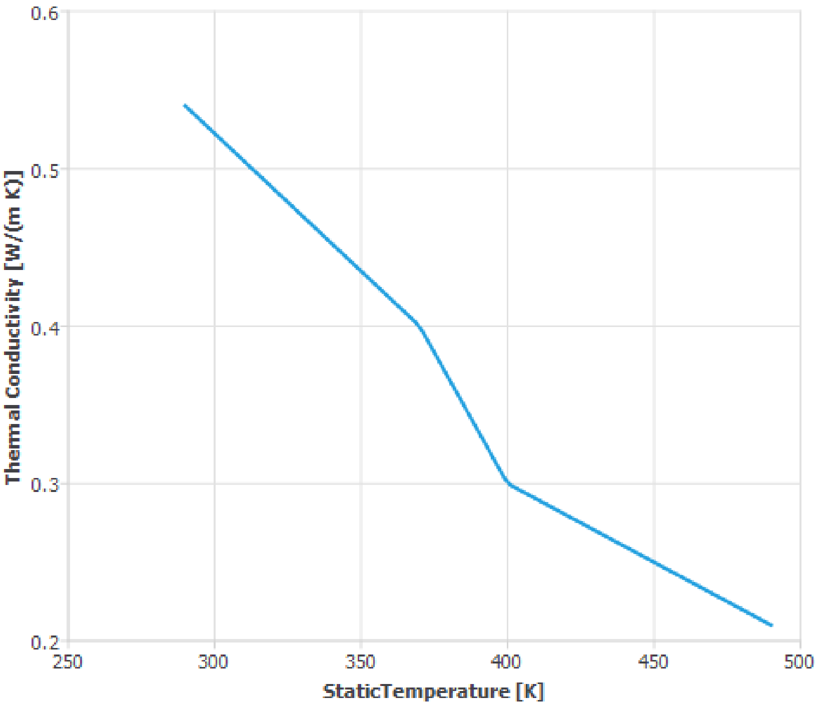

Figure C.2: Graph picturing the piece wise linear function of thermal conductivity for the HDPE.

C.3 Constant properties

Property	**Value**
Density	960 kg/m^3
Liquidus temperature	402 K
Solidus temperature	397 K
Heat of fusion	220 kJ/kg

Table C.3: Constant thermal properties for the high-density polyethylene

D Container Properties

Property	**Value**
Cast iron	
Density	7847 kg/m^3
Specific Heat Capacity	470 J/(kgK)
Thermal conductivity	50 W/(mK)
Aluminum	
Density	2719 kg/m^3
Specific Heat Capacity	871 J/(kgK)
Thermal conductivity	200 W/(mK)

Table D.1: Thermal properties for the aluminum and cast iron used in the numerical computations.

E Matlab Code from Channel Estimations

```
%% Constants and Variables
%Container
H       = 0.2;                              %[m] Height of container.
S       = linspace(0.01,0.025,150);%0.014;  %[m] Slit distance
R       = 0.253;                            %[m] Radius container
s       = 3*10^(-3);                        %[m] Thickness container wall
N       = [8 10 12 14 16 18];               % Number of fins
circ_i  = 2*pi*R;
circ_o  = 2*pi*(R+S);
circ_oo = 2*pi*(R+S+s);
A_s1    = circ_i*H;                         %[m^2] Surface area 1
A_s2i   = circ_o*H;                         %[m^2] Inner surface area 2
A_s2o   = circ_oo*H;                        %[m^2] Outer surface area 2
w       = N*s;                              %[m] Occupied width of fins
P       = 2*(s+H);                          %[m] Perimeter, one fin
A_c     = H*s;                              %[m^2] Cross section, one fin

epsilon = [0.8 0.8];
sigma   = 5.67*10^(-8);
k       = [50 200];
%Ambient
T_sur   = 273.15 + 20;                      %[K] Ambient temperature
T_s1    = 60;                               %[C] Temperature for plate 1
Tb      = T_s1 + 273.15;                    %[K] Base temperature fin
q_wo_rs_steel   = A_s1*(epsilon(1)*sigma*(Tb^2+T_sur^2)*(Tb+T_sur)+...
    (-1.0919e-08 *(Tb^4) + 1.8344e-05*(Tb^3) - 0.0115369579*(Tb^2) ...
    + 3.2296226295*Tb - 333.83090929))*(Tb-T_sur);
q_wo_rs_alu     = A_s1*(epsilon(2)*sigma*(Tb^2+T_sur^2)*(Tb+T_sur)+...
    (-1.0919e-08 *(Tb^4) + 1.8344e-05*(Tb^3) - 0.0115369579*(Tb^2) ...
    + 3.2296226295*Tb - 333.83090929))*(Tb-T_sur);
%% Table Air Properties
temp    = [250 300 350 400 450 500 550 600];                       %[K]
rho_a   = [1.3947 1.1614 0.995 0.8711 0.774 0.6964 0.6329 0.5804];%[kg/m^3]
cp_a    = [1006 1007 1009 1014 1021 1030 1040 1051];                %[J/kgK]
nu_a    = [1.44*10^(-5) 1.589*10^(-5) 2.092*10^(-5) 2.641*10^(-5) ...
         3.239*10^(-5) 3.879*10^(-5) 4.557*10^(-5) 5.269*10^(-5)]; %[m/s^2]
k_a     = [0.0223 0.0263 0.03 0.0338 0.0373 0.0407 0.0439 0.0469]; %[W/mK]

%% Inlet
%Air properties
for a = 1:length(temp)
    if T_sur    >   temp(a)    &&    T_sur   <=  temp(a+1)
        x_in    = (T_sur-temp(a))/(temp(a+1)-temp(a));
        rho_in  = x_in*(rho_a(a+1)-rho_a(a))+rho_a(a);
        cp_in   = x_in*(cp_a(a+1)-cp_a(a))+cp_a(a);
        nu_in   = x_in*(nu_a(a+1)-nu_a(a))+nu_a(a);
        k_in    = x_in*(k_a(a+1)-k_a(a))+k_a(a);
    end
end

%% Calculation process
count = 0;
for aa=1:length(k)  %For loop for each material
    for i=1:length(N)
```

```
        for j=1:length(S)
            A_ch(i,j)   = 2*S(j)*H + (circ_i-w(i) + circ_o(j)-w(i))*H/N(i);
%[m^2] Surface area inside one channel
            L_f(i,j)    = (S(j) + ((circ_o(j)+circ_oo(j))/2)/(N(i)*2));
%[m] Length to one "fin".
            A_c_ch(i,j) = ((pi*((R+S(j))^2-R^2))/N(i)-s*S(j));
%[m^2] Cross section area of one channel
            D_h(i,j)    = 4 * A_c_ch(i,j)/(A_ch(i,j)/H);
% Dh=4A/P. Could maybe be simplified to 2*S.
            diff_q(i,j) = 20;

            %First guess of average external wall.
            T2(i,j)     = Tb;
            diff_T(i,j) = 50;

            %Iterating external wall temperature
            while (diff_T(i,j)) > 0.01
                %New guess T2
                T2(i,j) = T2(i,j)-0.001;
                To_g    = T2(i,j);
                To(i,j) = 300;
                % Iterating outlet air temperature
                while abs(To_g - To(i,j)) > 0.01
                    %New guess To
                    To_g    = To(i,j);
                    T_m(i,j)= (To_g+T_sur)/2;

                    % Air prop for mean temperature
                    for p = 1:length(temp)
                        if T_m(i,j) > temp(p) && T_m(i,j) <= temp(p+1)
                            x_m   = (T_m(i,j)-temp(p))/(temp(p+1)-temp(p));
                            rho_m = x_m*(rho_a(p+1)-rho_a(p))+rho_a(p);
                            cp_m  = x_m*(cp_a(p+1)-cp_a(p))+cp_a(p);
                            nu_m  = x_m*(nu_a(p+1)-nu_a(p))+nu_a(p);
                            k_m   = x_m*(k_a(p+1)-k_a(p))+k_a(p);
                        end
                    end

                    %Aspect ratio
                    Aspectratio(i,j)=((circ_o(j)-w(i))/N(i))/S(j);

                    AR      = [2 3 4 8 100];
                    Nu_T    = [3.39 3.96 4.44 5.60 7.54];
                    f_Re    = [62 69 73 82 96];

                        for n = 1:length(AR-1)
                            if Aspectratio(i,j) >= AR(n) && Aspectratio(i,j) < AR(n+1
                                Nu(i,j)  = (Aspectratio(i,j)-AR(n))/(AR(n+1)-AR(n))...
                                    *(Nu_T(n+1)-Nu_T(n))+Nu_T(n);
                                f(i,j)   = (Aspectratio(i,j)-AR(n))/(AR(n+1)-AR(n))...
                                    *(f_Re(n+1)-f_Re(n))+f_Re(n);
                            end
                        end

                    drho        = rho_m-rho_in;
                    DF(i,j)     = -drho*9.81*H;             %[N] Pressure difference
                    v(i,j)      = DF(i,j)*D_h(i,j)^2/(H*(f(i,j)/2)*nu_m*rho_m);
%[m/s] Drivingforce=Friction. Assuming infinite parallel plates. f=96/Re
```

```
                    Re(i,j)     = v(i,j)*D_h(i,j)/nu_m;
                    m_dot(i,j)  = rho_m*A_c_ch(i,j)*v(i,j); %Mass flow channel

                    %NTU-e
                    h_ch(i,j)   = Nu(i,j)*k_m/D_h(i,j);
                    NTU         = h_ch(i,j)*(A_ch(i,j))/(m_dot(i,j)*cp_m);
                    e           = 1-exp(-NTU);
                        %Fins (adiabatic tip)
                        hr(i,j)     = epsilon(aa)*sigma*...
                            (T2(i,j)^2+T_sur^2)*(T2(i,j)+T_sur);
                        hv(i,j)     = -1.0919e-08 *(T2(i,j)^4) ...
                                        + 1.83441e-05*(T2(i,j)^3) ...
                                        - 0.0115369579*(T2(i,j)^2) ...
                                        + 3.2296226295*T2(i,j) ...
                                        - 333.8309290914;
                        h_v_inf(i,j)= hr(i,j)+hv(i,j);
                        h_fin(i,j)  = (h_v_inf(i,j)+h_ch(i,j))/2;
                        m           = sqrt((h_fin(i,j)*P)/(k(aa)*A_c));
                        T_tip(i,j)  = 1/(cosh(m*L_f(i,j)))*(Tb-T_m(i,j))...
                                        + T_m(i,j);
%[K] Coldest part of the external wall (Mid channel)
                        T_mid(i,j)  = (cosh(m*(L_f(i,j)-S(j))))...
                            /(cosh(m*L_f(i,j))) *(Tb-T_m(i,j)) + T_m(i,j);
%[K] Hottest point of the external wall

                        A_f(i,j)    = (circ_o(j)+circ_oo(j)-w(i)...
                                        +S(j)*2*N(i))*H;
                        A(i,j)      = A_f(i,j) + (circ_i-w(i))*H;
                        eta_f(i,j)  = tanh(m*L_f(i,j))/(m*L_f(i,j));
                        eta_0(i,j)  = 1 - A_f(i,j)/A(i,j)*(1-eta_f(i,j));
                        T_avg(i,j)  = eta_f(i,j)*(Tb-T_sur)+T_sur;

                    To(i,j)     = T_sur+((T_avg(i,j)+Tb)/2-T_sur)*e;
                end
                diff_T(i,j)     = T2(i,j) - T_avg(i,j);

            end

                M(i,j)      = sqrt(P*h_fin(i,j)*k(aa)*A_c)*(Tb-T_m(i,j));
                q_f(i,j)    = M(i,j)*tanh(m*L_f(i,j))*N(i)*2;
                q2_inf(i,j) = (h_v_inf(i,j))*A_s2o(j)*(T_avg(i,j)-T_sur);
                q_ch(i,j)   = m_dot(i,j)*cp_m*(To(i,j)-T_sur)*N(i);

                q_RS_1      = q2_inf(i,j)/N(i);
                q_air_1     = q_ch(i,j)/N(i);

                %Top
                T_top_C     = (100-30)/(150-30)*(Tb-273.15);%Experimental correlation
                T_top(i,j)  = T_top_C+273.15;
                h_top_r(i,j)= (epsilon(aa)*sigma*(T_top(i,j)^2+T_sur^2)...
                                *(T_top(i,j)+T_sur));
                h_h(i,j)    = (-1.435*10^(-8))*(T_top(i,j)^4)...
                                +(2.41634*10^(-5))*(T_top(i,j)^3)...
                                -0.01522994832*(T_top(i,j)^2)...
                                +4.2741550615*T_top(i,j)...
                                -442.9628494225;
                h_top(i,j)  = h_top_r(i,j) + h_h(i,j);
                q_top(i,j)  = h_top(i,j)*pi*R^2*(T_top(i,j)-T_sur);

                q_tot(i,j)  = q_ch(i,j) + q2_inf(i,j) + q_top(i,j);

                %Entry length
                entrylength_therm(i,j)  = 0.05*Re(i,j)*nu_m/...
                                            (k_m/(rho_m*cp_m))*D_h(i,j);
                entrylength_hydr(i,j)  = 0.05*Re(i,j)*D_h(i,j);
        end
    end
end
```

F Effective Conductivity for Air Void in Storage

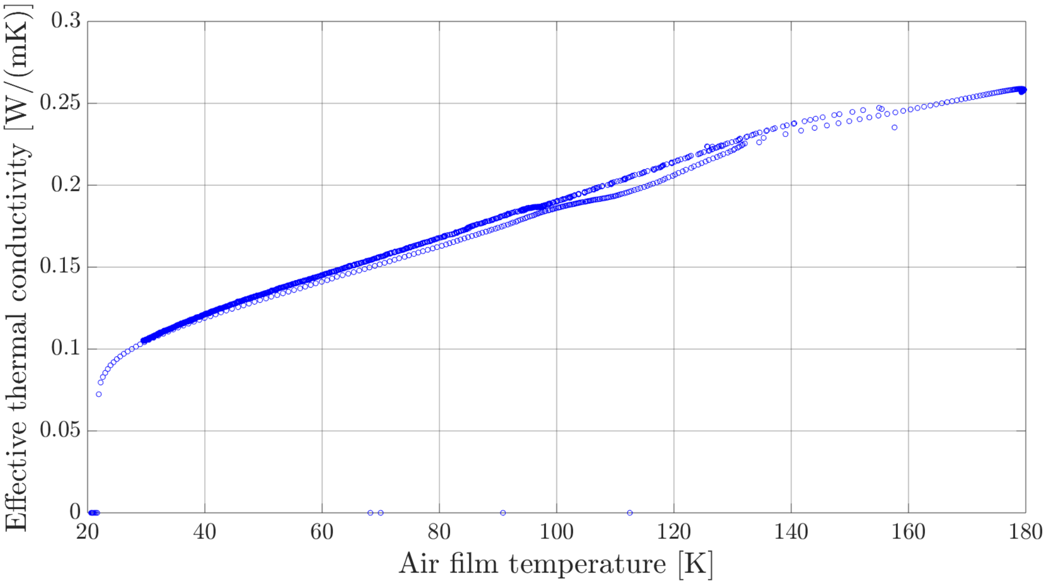

Figure F.1: Expression for effective thermal conductivity for the air void represented as a solid in the numerical computations. This was derived from experimental data.

$$k(T) = \begin{cases} 0.025, & \text{if } T < 290 \\ 0.0075(T-290) + 0.025, & \text{if } 300 > T \geq 290 \\ 0.00104(T-300) + 0.1, & \text{if } 500 > T \geq 300 \end{cases}$$

G Proportional Relations for Natural Convection

The proportionality between the effective thermal conductivity obtained for the PCM experiencing natural convection and the characteristic length will be derived in the next section. A graph plotting the proportionality constants for each numerical results is pictured after the derivation.

G.1 Derivation

For laminar flow, where natural convection appears when heat is added at the bottom, the Nusselt number is proportional to the Rayleigh number to the power of one fourth.

$$Nu \propto Ra^{1/4}$$

Rayleigh number is proportional to characteristic length to the power of three.

$$Ra \propto L_c^3.$$

This leads to

$$Nu \propto L_c^{3/4}.$$

Since the Nusselt number is defined as

$$Nu = \frac{hL_c}{k},$$

one obtain the proportionality

$$L^{3/4} \propto \frac{hL_c}{k}.$$

To extract the effective thermal conductivity, k_{eff}, Fourier's law was used. Setting this equal to Newton's law of cooling, a relation between the heat transfer coefficient and effective thermal conductivity may be found.

$$q'' = k_{eff}\frac{\Delta T}{L_c} = h\Delta T \implies k_{eff} = hL_c$$

By substituting hL_c with k_{eff} in the last proportionality, the final proportionality between the relative thermal conductivity, k_r, and characteristic length, L_c, is finally found to be

$$k_r = \frac{k_{eff}}{k} \propto L_c^{3/4}$$

G.2 Plot of the Obtained Constants

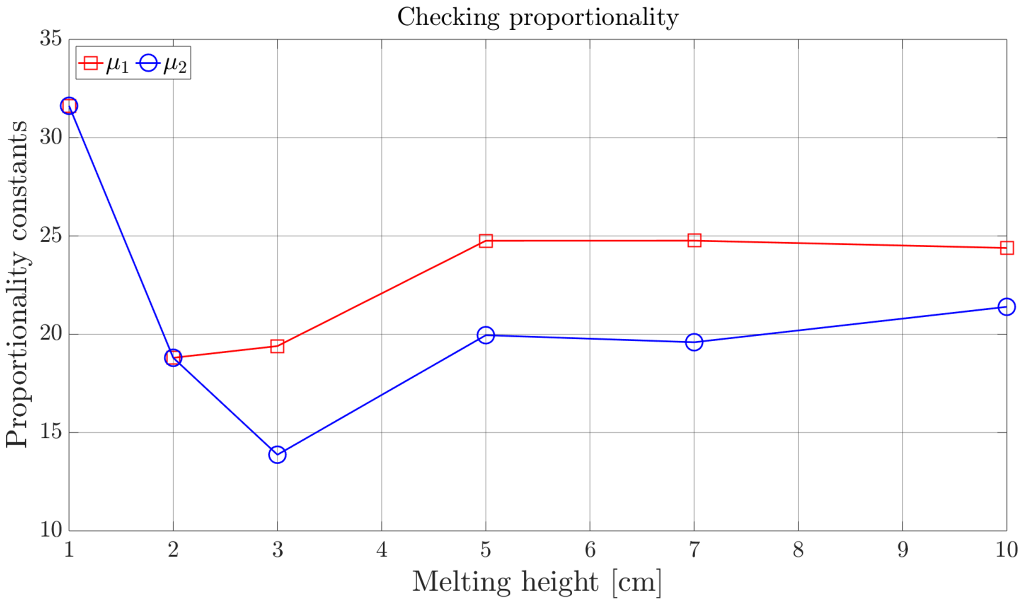

Figure G.1: Every single proportionality constant for the relative thermal conductivity and characteristic length. A constant is computed for each simulated scenario. They are calculated from the numerical results obtained in chapter 5.

NTNU

Norwegian University of
Science and Technology